Princeton Plasma Physics Laboratory

PPPL-4211

PPPL-4211

# Overview of Recent Physics Results from the National Spherical Torus Experiment (NSTX)

J.E. Menard, M.G. Bell, R.E. Bell, S. Bernabei,
J. Bialek, T. Biewer, et al.

January 2007

Prepared for the U.S. Department of Energy under Contract DE-AC02-76CH03073.

# Princeton Plasma Physics Laboratory
# Report Disclaimers

---

## Full Legal Disclaimer



## Trademark Disclaimer



---

# PPPL Report Availability

## Princeton Plasma Physics Laboratory:

http://www.pppl.gov/pub_report/

## Office of Scientific and Technical Information (OSTI):

http://www.osti.gov/bridge

## U.S. Department of Energy:

U.S. Department of Energy
Office of Scientific and Technical Information
P.O. Box 62
Oak Ridge, TN 37831-0062
Telephone: (865) 576-8401
Fax: (865) 576-5728
E-mail: reports@adonis.osti.gov

# Overview of Recent Physics Results from the National Spherical Torus Experiment (NSTX)

J.E. Menard[1], M.G. Bell[1], R.E. Bell[1], S. Bernabei[1], J. Bialek[2], T. Biewer[1], W. Blanchard[1], J. Boedo[3], C.E. Bush[4], M.D. Carter[4], W. Choe[5], N.A. Crocker[6], D.S. Darrow[1], W. Davis[1], L. Delgado-Aparicio[7], S. Diem[1], C.W. Domier[8] D.A. D'Ippolito[9], J. Ferron[10], A. Field[11], J. Foley[1], E.D. Fredrickson[1], D.A. Gates[1], T. Gibney[1], R. Harvey[12], R.E. Hatcher[1], W. Heidbrink[13], K.W. Hill[1], J.C. Hosea[1], T.R. Jarboe[14], D.W. Johnson[1], R. Kaita[1], S.M. Kaye[1], C.E. Kessel[1], S. Kubota[6], H.W. Kugel[1], J. Lawson[1], B.P. LeBlanc[1], K.C. Lee[8], F.M. Levinton[15], N.C. Luhmann, Jr.[8], R. Maingi[4], R.P. Majeski[1], J. Manickam[1], D.K. Mansfield[1], R. Maqueda[15], R. Marsala[1], D. Mastrovito[1], T.K. Mau[3], E. Mazzucato[1], S.S. Medley[1], H. Meyer[11], D.R. Mikkelsen[1], D. Mueller[1], T. Munsat[16], J.R. Myra[9], B.A. Nelson[14], C. Neumeyer[1], N. Nishino[17], M. Ono[1], H.K. Park[1], W. Park[1], S.F. Paul[1], T. Peebles[6], M. Peng[4], C. Phillips[1], A. Pigarov[3], R. Pinsker[10], A. Ram[18], S. Ramakrishnan[1], R. Raman[14], D. Rasmussen[4], M. Redi[1], M. Rensink[19], G. Rewoldt[1], J. Robinson[1], P. Roney[1], A.L. Roquemore[1], E. Ruskov[13], P. Ryan[4], S.A. Sabbagh[2], H. Schneider[1], C.H. Skinner[1], D.R. Smith[1], A. Sontag[2], V. Soukhanovskii[19], T. Stevenson[1], D. Stotler[1], B.C. Stratton[1], D. Stutman[7], D. Swain[4], E. Synakowski[1], Y. Takase[20], G. Taylor[1], K. Tritz[7], A. von Halle[1], M. Wade[10], R. White[1], J. Wilgen[4], M. Williams[1], J.R. Wilson[1], H. Yuh[15], L.E. Zakharov[1], W. Zhu[2], S.J. Zweben[1], R. Akers[11], P. Beiersdorfer[19], R. Betti[21], T. Bigelow[4], M. Bitter[1], P. Bonoli[18], C. Bourdelle[22], C.S. Chang[23], J. Chrzanowski[1], L. Dudek[1], P.C. Efthimion[1], M. Finkenthal[7], E. Fredd[1], G.Y. Fu[1], A. Glasser[24], R.J. Goldston[1], N.L. Greenough[1], L.R. Grisham[1], N. Gorelenkov[1], L. Guazzotto[21], R.J. Hawryluk[1], J. Hogan[4], W. Houlberg[4], D. Humphreys[10], F. Jaeger[4], M. Kalish[1], S. Krasheninnikov[3], L.L. Lao[10], J. Lawrence[25], J. Leuer[10], D. Liu[13], G. Oliaro[1], D. Pacella[26], R. Parsells[1], M. Schaffer[10], I. Semenov[27], K.C. Shaing[28], M.A. Shapiro[18], K. Shinohara[29], P. Sichta[1], X. Tang[24], R. Vero[7], M. Walker[10], and W. Wampler[30]

[1] Princeton Plasma Physics Laboratory, Princeton University, Princeton, NJ 08543, USA
[2] Department of Applied Physics, Columbia University, NYC, NY, USA
[3] University of California, San Diego, CA, USA
[4] Oak Ridge National Laboratory, Oak Ridge, TN, USA
[5] Korea Advanced Institute of Science and Technology, Taejon, Korea
[6] University of California, Los Angeles, CA, USA
[7] Johns Hopkins University, Baltimore, MD, USA
[8] University of California, Davis, CA, USA
[9] Lodestar Research Corporation, Boulder, CO, USA
[10] General Atomics, San Diego, CA, USA
[11] Euratom-UKAEA Fusion Associates, Abingdon, Oxfordshire, UK
[12] Comp-X, Del Mar, CA, USA
[13] University of California, Irvine, CA, USA
[14] University of Washington, Seattle, WA, USA
[15] Nova Photonics, Princeton, NJ, USA
[16] University of Colorado, Boulder, CO, USA
[17] Hiroshima University, Hiroshima, Japan
[18] Massachusetts Institute of Technology, Cambridge, MA, USA
[19] Lawrence Livermore National Laboratory, Livermore, CA, USA

[20] University of Tokyo, Tokyo, Japan
[21] University of Rochester, Rochester, NY, USA
[22] CEA, Cadarache, France
[23] New York University, NYC, NY, USA
[24] Los Alamos National Laboratory, Los Alamos, NM, USA
[25] Princeton Scientific Instruments, Princeton, NJ, USA
[26] ENEA, Frascati, Italy
[27] Kurchatov Institute, Russia
[28] University of Wisconsin, Madison, WI, USA
[29] JAERI, Naka, Japan
[30] Sandia National Laboratory, Albuquerque, NM, USA
email-contact of main author: jmenard@pppl.gov

**Abstract** - The National Spherical Torus Experiment (NSTX) has made considerable progress in advancing the scientific understanding of high performance long-pulse plasmas needed for future Spherical Torus (ST) devices and ITER. Plasma durations up to 1.6s (5 current redistribution times) have been achieved at plasma currents of 0.7 MA with non-inductive current fractions above 65% while simultaneously achieving $\beta_T$ and $\beta_N$ values of 17% and 5.7 (%m·T/MA), respectively. A newly available Motional Stark Effect diagnostic has enabled validation of current drive sources and improved the understanding of NSTX "hybrid"-like scenarios. In MHD research, ex-vessel radial field coils have been utilized to infer and correct intrinsic error fields, provide rotation control, and actively stabilize the $n$=1 resistive wall mode at ITER-relevant low plasma rotation values. In transport and turbulence research, the low aspect ratio and wide range of achievable $\beta$ in NSTX are providing unique data for confinement scaling studies, and a new microwave scattering diagnostic is investigating turbulent density fluctuations with wavenumbers extending from ion to electron gyro-scales. In energetic particle research, cyclic neutron rate drops have been associated with the destabilization of multiple large Toroidal Alfven Eigenmodes (TAEs) similar to the "sea-of-TAE" modes predicted for ITER, and three-wave coupling processes have been observed for the first time. In boundary physics research, advanced shape control has enabled studies of the role of magnetic balance in H-mode access and ELM stability. Peak divertor heat flux has been reduced by a factor of 5 using an H-mode-compatible radiative divertor, and lithium conditioning has demonstrated particle pumping and results in improved thermal confinement. Finally, non-solenoidal plasma start-up experiments have achieved plasma currents of 160kA on closed magnetic flux surfaces utilizing Coaxial Helicity Injection.

## 1. Progress in Plasma Performance and Understanding

The National Spherical Torus Experiment (NSTX) [1, 2] has made considerable progress in advancing the scientific understanding of high performance long-pulse plasmas needed for low-aspect-ratio spherical torus (ST) [3] concepts and for ITER. Several new tools [4] have aided this progress including: modified divertor poloidal field coils for combined high triangularity and high elongation [5], a Motional Stark Effect diagnostic operable at low magnetic field strength [6], and six mid-plane ex-vessel coils producing controllable radial magnetic field perturbations for rotation control [7], error field correction [4], and resistive wall mode (RWM) control at ITER-relevant low plasma rotation values [8].

As shown in Figure 1a, plasma flat-top durations approaching 5 current redistribution times [9] and 50 energy confinement times have been achieved with the product of normalized beta and confinement enhancement, $\beta_N H_{89P}$, in the range needed for an ST-based Component Test Facility (CTF) [10]. The longest discharge pulse-length achieved to-date using up to 7MW of Neutral Beam Injection (NBI) heating is 1.6s - a 60% increase relative to 2004. These discharges have flat-top plasma currents of 0.7 MA with peak non-inductive (NI) current fractions $f_{NI} \leq 65\%$ while simultaneously achieving $\beta_T \leq 17\%$ and $\beta_N \leq 5.7$(%m·T/MA), respectively [11]. This performance has been achieved by operating with increased boundary triangularity at high elongation utilizing advanced shape control [12], from a reduction in the severity of Edge-Localized Modes (ELMs) at high elongation by operating with slightly negative magnetic balance [5, 13] and operation above the ideal no-wall stability limit and near the ideal-wall stability limit [14, 15, 16] via rotational stabilization of the RWM. NSTX now routinely operates with sustained boundary elongation of 2.4-2.5, and as is evident from Figure 1b, can stably access significantly higher elongation with a peak value of 3 achieved in 2006 [17]. Since $f_{BS} \propto \sqrt{\epsilon}(1+\kappa^2)\beta_N^2/\beta_T$, increased elongation is a primary means of increasing the bootstrap fraction while maintaining high $\beta_T$. As seen in Figure 1c, the highest performance NSTX plasmas are very close to simultaneously achieving $\beta_T = 20\%$ and $f_{BS} = 50\%$ projected to be required for a ST-CTF.

The longest duration discharges of NSTX described above often maintain central $q$ above unity for many current redistribution times. Improved understanding of this physics may offer insight into mechanisms that sustain the "hybrid" scenario proposed as a possible improved high-Q scenario for ITER [18]. Such studies have been enabled by a 12 channel MSE diagnostic operable at the low toroidal fields of NSTX [6].

Figure 2a compares the measured total plasma current to the predicted current from both inductive and non-inductive sources. Here, the loop voltage profiles are computed directly from the MSE-constrained reconstructions, the inductive and bootstrap currents are calculated using Sauter's formulas [19], and the NBI current drive (NBICD) is computed using TRANSP [20]. For discharges that are sufficiently MHD-quiescent, the measured and predicted total currents and neutron rates typically agree to within 5-10%. As seen in Figure 2b, the reconstructed and predicted plasma current density profiles are also in good agreement with NBICD dominating the non-inductive current drive in the plasma core, and bootstrap (BS) current dominating off-axis. During the highest $\beta_N = 5.5$-6 phase of such discharges, the plasma is typically near the ideal-wall limit, and repeated excursions above this limit have been observed to trigger saturated core-localized $n$=1 interchange-type instabilities [11]. During such MHD activity, discrepancies as large as 40% between the reconstructed and predicted core current density have been observed.

Significant deviations between the predicted and measured fast-particle distributions are also evident in the neutron rate and Neutral Particle Analyzer (NPA) data [21]. Agreement between measurement and prediction is significantly improved if the $n$=1 mode is assumed to cause significant NBI fast-particle redistribution in the plasma core with moderate global loss < 15%. As seen in Figure 2c, such redistribution can apparently convert a centrally-peaked NBICD profile into a flat or even hollow profile. For a discharge similar to that shown in Figure 2 but with earlier $n = 1$ mode onset near t=0.6s, Figure 3 shows the (a) time-dependent profiles and (b) energy dependence of the anomalous fast ion diffusion (AFID) needed to match (c) the energy distribution and (d) magnitude of the NPA signal in the presence of the MHD activity. With this AFID model included, the reconstructed core current density profile is in much better agreement with prediction [21], again consistent with MHD activity redistributing the NBI-driven current.

Validation of non-inductive current drive sources in the absence of large-scale MHD activity has also enabled identification of fully non-inductive scenarios extrapolated from present discharge parameters as shown in Figure 2 [22]. Fully non-inductive $I_P = 700$kA, $B_T = 5.2$kG scenarios are calculated to be achievable by increasing the thermal temperatures 50-70%, decreasing the electron density 25%, increasing elongation from 2.3 to 2.6 and bottom triangularity from 0.75 to 0.85. Self-consistent profiles for such a scenario are shown in Figure 4. The necessary increase in $\beta_N$ from 5.6 to 6.7 would require either enhanced confinement from lithium wall conditioning as described in Section 5, and/or efficiently coupled High-harmonic Fast-Wave (HHFW) heating as described in Section 6. This increased $\beta_N$ scenario is calculated to be $n$=1-3 ideal-wall stable for the predicted increase in $q_{min}$ to 2.4 from 1.3 and would require RWM stabilization either from plasma rotation and dissipation and/or active feedback control.

## 2. Macroscopic stability

In most high-$\beta_N$ scenarios in NSTX operating above the no-wall stability limit, RWM stabilization is achieved passively from high plasma rotation due to unidirectional tangential NBI heating. However, some discharge scenarios exhibit rotation slow-down at radii near the $q$=2 and 3 surfaces and suffer rapid collapses in $\beta$. Six mid-plane ex-vessel coils (RWM/EF coils) producing controllable $n$=1 and/or $n$=3 radial magnetic fields have been commissioned on NSTX and utilized to study error field (EF) and RWM physics in detail. Real-time measurement and closed-loop feedback-control of low-frequency MHD activity including unstable RWMs and error fields amplified by the stable RWM have also been implemented on NSTX.

Low-density locked-mode threshold experiments have identified $n$=1 resonant error fields of 1-3 Gauss [4] calculated at the $q$=2 surface near $\rho_{pol} \equiv \sqrt{\hat{\psi}_{pol}} = 0.7$-0.8. After subtracting the inferred intrinsic error field from total applied field at locking, the density dependence of the 2/1 locked-mode threshold scales as $\bar{n_e}^{0.93}$ as shown in Figure 5a for $I_P$=700kA, $B_T$=0.45T lower-single-null discharges. This threshold scaling is very nearly linear in density consistent with theory expectations and results from higher aspect ratio tokamaks [23, 24].

Additional experiments at higher $\beta$ revealed error fields of similar magnitudes but of opposite polarity. The source of this error field has since been traced to motion of the toroidal field (TF) central conductor bundle relative to the vacuum vessel and poloidal

field (PF) coils induced by the ohmic heating (OH) solenoid. The error field is measured to be proportional to the time-delayed and partially-rectified product of the OH and TF coil currents. Thus, the error field changes sign due to the double-swing OH transformer current passing through zero.

Using the improved understanding of the intrinsic error field source, the low and high $\beta$ locking data together also revealed that minimizing the 2/1 component of the vacuum error field at the computed 2/1 surface inside the plasma does not give optimal correction, i.e. the minimization of flow damping. The $m$=0 component of the vacuum error field is found to be significant for the TF shift, and this component also has a polarity opposite to the other $|m| > 0$ components. As shown in Figure 5b, balancing the $m$=0 against the $m$=2 component can empirically provide a nearly invariant threshold field of $\approx 2$ Gauss for both data sets when the fields are added in quadrature. This result may imply the non-resonant $m$=0 component of the flow-damping is very important [25], or that the ideal plasma response to the error field is much different than the vacuum response.

Correction of this error field has been attempted using several control methods. First, as seen in Figure 6, correction of the OH×TF error-field (black curves) utilizing a real-time estimate of the TF coil motion increases the pulse duration above the no-wall limit by approximately 50% relative to no correction (red curves) during the high $\beta_N$ phase. As seen in the same figure, the addition (green curves) of gain and phase-optimized closed-loop feedback control of the measured in-vessel $n$=1 poloidal field to OH×TF correction can double the duration above the no-wall limit. Additional tests in these discharges find that closed-loop $n$=1 feedback alone does not provide robust pulse extension early in the high-$\beta_N$ phase, and that the OH×TF correction is not yet optimized late in the high-$\beta_N$ phase. Finally, using the time-average of the OH×TF plus closed-loop $n$=1 feedback coil currents (blue curves) provides nearly identical performance as the non-averaged coil currents. Because the measured RWM growth time (see below) is much shorter than the averaging time used in these experiments, this result implies that the feedback control system is responding to plasma induced error-field amplification and is aiding in sustaining the plasma rotation which stabilizes the RWM, rather than feeding back directly on the unstable RWM. Similar results have also been obtained on DIII-D [26]. Further, these results are consistent with low-frequency MHD spectroscopy measurements [27] indicating the presence of a stable $n$=1 RWM resonant at $30 - 50$Hz in the co-rotation direction [28] as shown in Figure 7.

The same RWM/EF control coils used for error field correction studies have also been used to investigate magnetic braking physics and feedback stabilization of the RWM. Rotation damping from both $n$=1 and $n$=3 fields has been compared to Neoclassical Toroidal Viscosity (NTV) theory. Figure 8a shows an example of the good agreement between the measured and predicted torques for $n$=3 radial magnetic fields applied by the RWM/EF coils [7]. Both $n$=1 and $n$=3 applied fields have been shown capable of lowering the plasma rotation to values below the RWM critical rotation frequency. However, the non-resonant $n$=3 field is most commonly used for magnetic braking when studying the $n$=1 RWM to minimize complications in measuring and interpreting $n$=1 RWM growth. This technique has been used to measure the $n$=1 critical rotation frequency [15, 28] and has allowed controlled experiments on $n$=1 RWM feedback stabilization at ITER-relevant low plasma rotation levels [8]. The black curve in Figure 8b illustrates the undamped rotation profile typical of the rotationally-stabilized plasmas in these experiments, while the red and green curves show the rotation profiles at $n$=1 RWM marginal stability and dur-

ing RWM closed-loop feedback control, respectively. As seen in the figure, the rotation during feedback is approximately 1/3 of the critical value and is below the normalized rotation value predicted for ITER. Figures 8c and d show that feedback control of the RWM (black curves) can extend the duration of high $\beta_N$ above the no-wall limit by over 90 RWM growth times while the plasma rotation is maintained below the experimentally determined critical rotation frequency. This low rotation is sustained by steady $n$=3 braking from the nearly constant RWM/EF coil currents as illustrated in Figure 8e. Finally, Figure 8f shows the $n$=1 mode poloidal field as measured by the in-vessel RWM/EF sensor array with (black) and without (red) close-loop RWM control enabled demonstrating the suppression of RWM $n$=1 field by the feedback system. The results above improve the prospects for robust error field and RWM control at high $\beta_N$ in ITER and other magnetic fusion concepts operating above the no-wall ideal-stability limit.

## 3. Transport and Turbulence

The low aspect ratio and wide range of $\beta$ values accessible in NSTX ($\beta_T$ up to 40%) provide unique data for understanding the dependence of energy confinement on these parameters for the ST and for ITER. Initial H-mode energy confinement scaling studies for NSTX found a weaker dependence on plasma current than at conventional aspect ratio and a stronger dependence on $B_T$ [29]. NSTX H-mode confinement data has also been incorporated into international confinement databases, and resulting scalings using this and higher aspect ratio data indicate a stronger positive inverse aspect ratio dependence and weaker $\beta$ dependence than in the commonly used ITER98PB(y,2) scaling. More recent experiments have elucidated the distinct roles of ion and electron thermal transport in the global energy confinement scaling [30]. In particular, increasing the toroidal magnetic field from 0.35T to 0.55T results in a broadening of the electron temperature profile and a reduction in $\chi_e$ in the outer half of the plasma minor radius. Interestingly, the central electron temperature is observed to increase only 10-20% during this scan. As the plasma current is increased from 0.7-1.0MA, the ion transport is reduced the outer half of the plasma minor radius consistent with $\chi_i \approx \chi_{i-neoclassical}$. Thus, the electron transport largely determines the toroidal field scaling, while the ion (neoclassical) transport largely determines the plasma current scaling [30].

In the NSTX H-modes described above, the electron energy transport is anomalous. To investigate possible causes of anomalous electron transport, a 1mm microwave scattering diagnostic capable of measuring electron gyro-radius-scale turbulence has been implemented on NSTX. Figure 9a shows a top-down view of the microwave ray paths for scattered rays accepted by the collection waveguides of the system. The 280GHz system provides high radial spatial resolution $<$ 6cm, high $k$ resolution $<$ 1cm$^{-1}$, the ability to scan radially from near the magnetic axis to near the edge, and measures predominantly $k_r$ from 2-24cm$^{-1}$ covering ion to electron-scale turbulence. Data from this diagnostic will provide strong tests of anomalous electron energy transport theories - of particular importance to developing a first-principles predictive capability for electron energy transport for ITER and magnetic confinement devices in general. The availability of MSE data has also improved understanding of the role of magnetic shear in energy transport. In particular, reversed magnetic shear has been demonstrated to allow the formation of electron energy transport barriers in L-mode discharges, and electron energy confinement improvement correlates with the degree of measured magnetic shear reversal [2, 4, 30].

These high-$T_e \leq$ 2keV L-mode discharges are typically heated with one NBI source ($P_{NBI}$ =1.6-2MW) and achieve some of the highest transient energy confinement times in NSTX of $\tau_E$=80-100ms but have low $\beta_N$ limits $\leq 4$ and low non-inductive current fractions relative to the positive shear $T_e \leq$ 1.2keV H-mode discharges heated with 4-7MW as described in Section 1. Analysis of high-$k$ density fluctuation amplitude as a function of core magnetic shear in high-$T_e$ L-mode discharges does indicate some dependence on magnetic shear, but firm conclusions cannot yet be drawn. However, other discharge scenarios do show clear correlations between reduced transport and reduced density fluctuation amplitudes. With the high-$k$ system viewing at large major radius (see black oval in Figure 9a), Figure 9b shows a large reduction in fluctuation levels after the transition from L-mode to H-mode for nearly all radial wavenumbers measurable by the system.

Figure 10 shows linear micro-instability growth-rate calculations from the GS2 code [31] for plasma parameters at the radial position circled in Figure 9a for the discharge shown in Figure 9b during the L-mode and H-mode phases. As seen in Figure 10, ITG/TEM and ETG modes are unstable but have reduced growth rates after the transition from L-mode to H-mode. This decrease is consistent with the observed decrease in fluctuation levels for nearly all measured wavenumbers. During the H-mode phase, the $E \times B$ shearing rate exceeds the linear growth rate of the low-$k_\theta$ turbulence, non-linear simulations find that low-$k_\theta$ turbulence in the ITG/TEM range is suppressed, and consistent with this, the measured ion thermal diffusivity is at the neoclassical level [30]. Interestingly, as is evident in Figure 9b, unlike the lower-$k$ data, the highest $k_r = 24$ cm$^{-1}$ signal exhibits amplitude bursts during H-mode which correlate with ELM events. Present studies are attempting to determine if these bursts correspond directly to ELM-induced density perturbations of short radial scale-length, or are instead due to beam refraction effects.

Beyond the passive observation of transport properties, lithium-pellet-induced edge temperature perturbations have allowed the core electron transport response to be probed, and the two kinds of discharges described above exhibit very different transport responses. Figure 11a shows the electron temperature evolution in a positive shear H-mode discharge ($P_{NBI}$=5.5MW, $I_P$=0.7MA, $B_T$=0.45T) using two-color Ultra-Soft X-Ray (USXR) tomography [32]. Following the pellet perturbation, the core electron temperature gradient scale-length shown in Figure 11b is essentially constant indicating very stiff profiles consistent with the existence of a critical temperature gradient. In contrast, Figure 11c shows that the core electron temperature actually increases in L-mode ($P_{NBI}$=2MW, $I_P$=1MA, $B_T$=0.45T) after pellet injection, and Figure 11d indicates a significant increase in normalized temperature gradient and an apparent lack of profile stiffness. The ability to create and diagnose scenarios with large variations in electron transport while largely suppressing ion turbulence makes NSTX particularly well-suited for studying electron transport physics.

## 4. Energetic Particle Physics

NSTX is also well suited to investigate fast-ion driven instabilities and their influence on fast particle confinement for both ITER and STs. NBI-heated NSTX plasmas can match and exceed the fast-ion $\beta$ and velocity ratio $v_{fast}/v_{Alfven}$ of ITER (albeit at much higher fast-ion $\rho_*$) with complete diagnostic coverage including MSE. Cyclic neutron rate drops have been associated with the destabilization of multiple large Toroidal Alfven Eigenmodes (TAEs) similar to the "sea-of-TAEs" predicted for ITER, albeit at lower

TAE toroidal mode number $n$=1-6 [33]. NPA data shows the strongest particle density modulation occurs below the injection half-energy and that the density of the highest energy ions is modulated by roughly 10% [21]. Figure 12 compares the mode frequencies, fluctuation amplitudes, and neutron rate decrements (fast-ion loss) during single-mode and multi-mode TAE burst events. An important finding evident in this figure is that multi-mode burst events lead to 5× higher fast-ion losses than single-mode events despite having 2-3× lower RMS B-field fluctuation amplitude (0.15-0.2G vs. 0.3-0.5G). This data implies that the structure and multiplicity of TAE modes is just as important as mode amplitude (if not more so) in determining the mode-induced fast ion transport. Interestingly, recent NSTX results indicate that multi-mode coupling is not constrained to a single class of fast-ion instability. Figure 13a shows that TAE modes can coexist with Energetic Particle Modes (EPMs), and bi-coherence analysis indicates that an $n$=1 EPM mode can couple to two higher-$n$ (and higher frequency) TAE modes through a three-wave coupling process [34]. In fact, the dominant EPM can drive the TAE amplitude envelope to be toroidally localized during mode propagation as shown in Figure 13b. The data in Figures 12 and 13 together imply that the structure, multiplicity, and non-linear coupling characteristics of multiple fast-ion instabilities could all play a role in determining fast-ion transport in future ST devices and ITER.

## 5. Boundary Physics

Improved understanding and control of both steady-state and transient heat fluxes to the divertor and other plasma facing components are essential for the successful operation of ITER and future ST devices such as an ST-CTF. Large transient heat loads from ELMs pose a serious risk to the divertor of next-step devices, and this has motivated research on developing small ELM regimes and complete ELM suppression using "edge-ergodization" coils [35]. Modest changes in ELM size and frequency have been achieved in NSTX using the RWM/EF coils, and additional analysis indicates that such ELM mitigation can be further optimized [36]. However, a small "Type-V" ELM regime with $\Delta W/W_{TOT} < 1\%$ has been discovered on NSTX [37], and accessibility to this regime has been characterized as a function of pedestal collisionality, $\beta_N$, and boundary shaping [38]. More recent studies indicate that access to this small-ELM regime may be possible at low pedestal collisionality at the high boundary shaping factors accessible in the ST, and more detailed measurements of Type V ELM structure and dynamics have been obtained [13]. ELM severity is also observed to be very sensitive to magnetic balance, i.e. proximity to a double-null boundary shape. Optimal ELM characteristics are typically obtained in a shape with negative bias, i.e. toward lower single null [5, 13]. Studies of these effects have been facilitated by the successful implementation of rt-EFIT and the precise boundary control it enables [12]. This shape control capability has also been exploited to enable similarity experiments with MAST and DIII-D investigating the dependence of the H-mode pedestal structure on aspect ratio. In these experiments, the boundary shape and electron collisionality ($\nu_e^*$) and normalized ion gyro-radius ($\rho_i^*$) at the top of the outboard pedestal are matched. The pedestal data from all three devices is presently being assessed to develop an improved understanding for reliably extrapolating from present experiments to the pedestal parameters expected in ITER [39].

Outside the pedestal, particle and energy transport in the scrape-off-layer are also being actively investigated both theoretically and experimentally. In particular, a two-region

model has been developed to study the effects of magnetic geometry and collisionality on edge turbulence and propagation of filamentary coherent structures (blobs) [40]. Figure 14a shows [41] reasonable agreement between the "blob" normalized velocity and size inferred from gas-puff-imaging data and the bounds predicted by the two-region theory. The NSTX edge reciprocating probe also measures the density fluctuations associated with the filamentary coherent structures [42]. As seen in Figure 14b, the probe is located on the outboard side of the plasma below the vertical midplane and can probe several centimeters inside the separatrix. As shown in Figure 14c-e, far inside the separatrix, density holes are commonly measured, a mixture of density holes and peaks is measured just inside the separatrix, and only density peaks are found in the scrape-off-layer (SOL). The correlation between density holes inside the plasma with density peaks in the SOL is an active area of experimental and theoretical study.

High steady-state heat flux levels also pose serious issues for future STs and ITER. In NSTX, reductions in peak divertor heat flux have been achieved using both detached and radiative divertor scenarios via gas puffing at the inner strike point and/or private flux region in lower single null discharges [43]. The inner strike point of NSTX divertor discharges is typically observed to be fully detached, while the outer strike point is attached [44]. With sufficient $D_2$ gas injection in the divertor, it is also possible to partially detach the outer strike point, but thus far this has led to deleterious MHD activity and loss of H-mode. However, with reduced gas input, a "radiative divertor" regime has been developed which also produces significant reductions in peak divertor heat flux. Figures 15a-b show that the required gas injection in the divertor has no apparent impact on H-mode confinement, while Figures 15c-d indicate a modest decrease in core carbon concentration and radiation. Importantly, Figures 15e-f show that the peak heat flux is reduced by a factor of 5 prior to the onset of $\beta$-limiting MHD present in both the reference and radiative divertor discharge. Recent experiments also indicate that the peak divertor heat flux is a strong function of heating power and plasma current [45].

Even with the divertor heat flux reduction techniques described above, solid plasma facing components (PFCs) may be incapable of handling the very high peak divertor heat fluxes projected for future fusion power reactors such as ARIES-AT [46] (14MW/m$^2$) or ARIES-ST [47] (33MW/m$^2$). Liquid metal divertors offer a possible solution to this heat flux problem, and following the success of liquid lithium for particle pumping [48] and peak heat flux mitigation in CDX-U, NSTX has also been pursuing a staged approach to lithium PFC development. Following success in demonstrating particle pumping with lithium pellet conditioning, NSTX has used a lithium evaporator to achieve more rapid coatings of PFCs [49]. As shown on the left-hand-side of Figure 16, the NSTX Li-evaporator was designed to provide broad coverage of the lower centerstack and divertor region. H-modes are observed to be the most challenging plasma scenarios to achieve density control using Li-evaporation. While strong pumping is observed early in such discharges, the density rate of rise later in the discharge is usually similar to that observed without Li-evaporation. Figure 16a shows the modest 10-15% density decrease achieved after lithium coating late in H-mode discharges. However, evaporated lithium has been observed to have a more pronounced effect on other discharge parameters. Figure 16b shows that Li-evaporation reduces the plasma $Z_{eff}$ by up to 35%, and as evident in Figures 16c and d, increases the electron and ion temperatures by up to 25% and 40% respectively. Lithium is observed to improve the H-mode confinement enhancement factor relative to ITER98PB(y,2) from HH = 1.08 to 1.28. Such thermal confinement enhancements improve the prospects for

achieving the fully non-inductive scenarios discussed in Section 1. Development of a liquid lithium divertor target is being considered for NSTX to provide both enhanced particle pumping and initial studies of high-heat-flux handling capability.

## 6. Solenoid-free current formation and ramp-up

To minimize the radial build and maintain low aspect ratio in future reactors, elimination of the central solenoid is highly desirable. Such elimination is only possible with alternative means of plasma current formation and ramp-up. Plasma current formation using Coaxial Helicity Injection (CHI) has recently demonstrated record values of closed-flux plasma current up to 160kA [50, 51]. Consistent with flux closure, Figure 17a shows that the plasma current persists after the CHI injector current ($I_{INJ}$) reaches zero at t=9ms, and further analysis indicates the plasma current decays inductively with a decay-rate consistent with the measured $T_e$ = 20-30eV. As seen in Figure 17b, after the injector current has been turned off and the open-field-line currents have decayed away, fast camera images exhibit light emission consistent with the reconstructed lower single null separatrix geometry. Later in the discharge, both the camera images and reconstructions show the plasma has detached from the lower divertor coil as evident in Figure 17c.

A key research goal is to extend CHI plasmas to higher $I_P$ and $T_e$. Recent Electron Bernstein Wave (EBW) emission measurements [17] indicate that EBW heating and current drive could ultimately contribute to this goal. HHFW heating has already demonstrated the ability of heating $I_P$=250kA ohmic plasmas from 200eV to 1.6keV in H-mode with $f_{BS}$ of up to 80% [22]. Thus, if higher-$T_e$ CHI target plasmas could be produced, HHFW should be capable of further heating and increasing $I_P$ through BS and FW current overdrive. However, parasitic losses from Parametric Decay Instabilities (PDI) [52] have previously been shown to increase in severity at the lower $k_{||}$ needed for HHFW current drive. More recently, as shown in Figure 18a, wave-fields far from the antenna have been measured to increase as $k_{||}$ is lowered. These measurements are consistent with enhanced surface wave excitation and losses at the very low cutoff density associated with low $k_{||}$. Both PDI and surface-waves are expected to be reduced at higher toroidal field and/or higher $k_{||}$. Taking advantage of this new understanding and operating at the highest allowable toroidal field = 0.55T, Figure 18b shows near record $T_e$ values approaching 4keV achieved with current-drive phasing. Previously, such high $T_e$ was only achievable with heating phasing ($k_{||}$=14m$^{-1}$) [53]. Importantly, these high temperatures obtained with current-drive phasing are achieved with a target plasma temperature of only 200eV, and it should be possible to heat even lower target plasma temperatures with heating phasing. Thus, the results above improve the prospects for utilizing wave heating and current ramp-up of CHI target plasmas to initiate high performance ST plasmas.

## 7. Summary

NSTX has made significant progress in achieving and understanding sustained high-performance operation above the ideal no-wall stability limit with high non-inductive current fraction and H-mode energy confinement ($HH_{98PB(y,2)} \geq 1$). NSTX research is contributing to improved understanding of energy confinement scaling and the underlying causes of anomalous energy transport, the effect of multiple fast-ion instabilities on energetic particle confinement, novel methods for particle and divertor heat flux control, and

solenoid-free plasma current formation and ramp-up physics. These results strengthen the scientific foundation for high performance operation in both ITER and future ST devices.

The author of this manuscript is supported by US-DOE contract DE-AC02-76CH03073.

# References

[1] ONO, M., KAYE, S. M., PENG, Y.-K. M., BARNES, G., BLANCHARD, W., et al., Nucl. Fus. **40** (2000) 557.

[2] KAYE, S., BELL, M., BELL, R., BERNABEI, S., BIALEK, J., et al., Nucl. Fus. **45** (2005) S168.

[3] PENG, Y.-K. M. and STRICKLER, D. J., Nucl. Fus. **26** (1986) 769.

[4] BELL, M. G., BELL, R. E., GATES, D. A., KAYE, S. M., KUGEL, H., et al., Nucl. Fus. **46** (2006) S565.

[5] GATES, D. A., MAINGI, R., MENARD, J., KAYE, S., SABBAGH, S. A., et al., Phys. Plasmas **13** (2006) 056122.

[6] LEVINTON, F., Bull. Am. Phys. Soc. **49** (2004) 221.

[7] ZHU, W., SABBAGH, S. A., BELL, R. E., BIALEK, J. M., BELL, M. G., et al., Phys. Rev. Lett. **96** (2006) 225002.

[8] SABBAGH, S. A., BELL, R. E., MENARD, J. E., GATES, D. A., SONTAG, A. C., et al., Phys. Rev. Lett. **97** (2006) 045004.

[9] MIKKELSEN, D. R., Phys. Fluids B **1** (1989) 333.

[10] PENG, Y.-K. M., FOGARTY, P. J., BURGESS, T. W., STRICKLER, D. J., NELSON, B. E., et al., Plasma Phys. and Contr. Fus. **47** (2005) B263.

[11] MENARD, J. E., BELL, R. E., GATES, D. A., KAYE, S. M., LEBLANC, B. P., et al., Phys. Rev. Lett. **97** (2006) 095002.

[12] GATES, D. A., FERRON, J. R., BELL, M., GIBNEY, T., JOHNSON, R., et al., Nucl. Fus. **46** (2006) 1723.

[13] MAINGI, R., BELL, M. G., FREDRICKSON, E. D., LEE, K. C., MAQUEDA, R. J., et al., Phys. Plasmas **13** (2006) 092510.

[14] MENARD, J. E., BELL, M. G., BELL, R. E., GATES, D. A., KAYE, S. M., et al., Phys. Plasmas **11** (2004) 639.

[15] SONTAG, A. C., SABBAGH, S. A., ZHU, W., BIALEK, J. M., MENARD, J. E., et al., Phys. Plasmas **12** (2005) 056112.

[16] SABBAGH, S. A., SONTAG, A. C., BIALEK, J. M., GATES, D. A., GLASSER, A. H., et al., Nucl. Fus. **46** (2006) 635.

[17] GATES, D. A., MAINGI, R., MENARD, J., KAYE, S., SABBAGH, S. A., et al., Paper EX/P1-3, this conference.

[18] LUCE, T. C. and DIII-D Team, Nucl. Fus. **45** (2005) S86.

[19] SAUTER, O., ANGIONI, C., and LIN-LIU, Y. R., Phys. Plasmas **6** (1999) 2834.

[20] GOLDSTON, R. J., MCCUNE, D. C., and TOWNER, H. H., J. Comput. Phys. **43** (1981) 61.

[21] MEDLEY, S. S., ANDRE, R., BELL, R. E., DARROW, D. S., FREDRICKSON, E. D., et al., Paper EX/P6-13, this conference.

[22] KESSEL, C. E., BELL, R. E., BELL, M. G., GATES, D. A., KAYE, S. M., et al., Phys. Plasmas **13** (2006) 056108.

[23] La Haye, R. J., FITZPATRICK, R., HENDER, T. C., MORRIS, A. W., SCOVILLE, J. T., et al., Phys. Fluids B **4** (1992) 2098.

[24] BUTTERY, R. J., DE'BENEDETTI, M., HENDER, T. C., and TUBBING, B. J. D., Nucl. Fus. **40** (2000) 807.

[25] LAZZARO, E., BUTTERY, R. J., HENDER, T. C., ZANCA, P., FITZPATRICK, R., et al., Phys. Plasmas **9** (2002) 3906.

[26] GAROFALO, A. M., STRAIT, E. J., JOHNSON, L. C., La Haye, R. J., LAZARUS, E. A., et al., Phys. Rev. Lett. **89** (2002) 235001.

[27] REIMERDES, H., CHU, M. S., GAROFALO, A. M., JACKSON, G. L., La Haye, R. J., et al., Phys. Rev. Lett. **93** (2004) 135002.

[28] SONTAG, A. C., SABBAGH, S. A., ZHU, W., MENARD, J. E., BELL, R. E., et al., Paper EX/7-2Rb, this conference.

[29] KAYE, S. M., BELL, M. G., BELL, R. E., FREDRICKSON, E. D., LEBLANC, B. P., et al., Nucl. Fus. **46** (2006) 848.

[30] KAYE, S. M., LEVINTON, F. M., STUTMAN, D., TRITZ, K., YUH, H., et al., Paper EX/8-6, this conference.

[31] KOTSCHENREUTHER, M., REWOLDT, G., and TANG, W. M., Comput. Phys. Commun. **88** (1995) 128.

[32] STUTMAN, D., TRITZ, K., DELGADO, L., FINKENTHAL, M., BELL, M., et al., Paper P5.120 in Proceedings of the 33rd EPS, Rome, 2006.

[33] FREDRICKSON, E. D., BELL, R. E., DARROW, D. S., FU, G. Y., GORELENKOV, N. N., et al., Phys. Plasmas **13** (2006) 056109.

[34] CROCKER, N. A., PEEBLES, W. A., KUBOTA, S., FREDRICKSON, E. D., KAYE, S. M., et al., Phys. Rev. Lett. **97** (2006) 045002.

[35] EVANS, T. E., MOYER, R. A., THOMAS, P. R., WATKINS, J. G., OSBORNE, T. H., et al., Phys. Rev. Lett. **92** (2004) 235003.

[36] YAN, L., EVANS, T. E., KAYE, S. M., and MAINGI, R., Nucl. Fus. **46** (2006) 858.

[37] MAINGI, R., TRITZ, K., FREDRICKSON, E. D., MENARD, J. E., SABBAGH, S. A., et al., Nucl. Fus. **45** (2005) 264.

[38] MAINGI, R., BUSH, C. E., FREDRICKSON, E. D., GATES, D. A., KAYE, S. M., et al., Nucl. Fus. **45** (2005) 1066.

[39] MAINGI, R., Paper IT/P1-12, this conference.

[40] MYRA, J. R., RUSSELL, D. A., and DIPPOLITO, D. A., Phys. Plasmas **13** (2006) 112502.

[41] MYRA, J. R., D'IPPOLITO, D. A., STOTLER, D. P., ZWEBEN, S. J., LEBLANC, B. P., et al., Phys. Plasmas **13** (2006) 092509.

[42] BOEDO, J. A., MAQUEDA, R. J., RUDAKOV, D. L., MCKEE, G. R., KUGEL, H., et al., Paper EX/P4-2, this conference.

[43] SOUKHANOVSKII, V. A., MAINGI, R., RAMAN, R., BELL, R. E., BUSH, C., et al., Paper EX/P4-28, this conference.

[44] SOUKHANOVSKII, V. A., MAINGI, R., ROQUEMORE, A. L., BOEDO, J., BUSH, C., et al., J. Nucl. Mater. **337-339** (2005) 475.

[45] MAINGI, R., BUSH, C. E., KAITA, R., KUGEL, H. W., ROQUEMORE, A. L., et al., J. Nucl. Mater. (2006), at press.

[46] NAJMABADI, F., ABDOU, A., BROMBERG, L., BROWN, T., CHAN, V. C., et al., Fus. Engin. and Design **80** (2006) 3.

[47] JARDIN, S. C., KESSEL, C. E., MENARD, J., MAU, T. K., MILLER, R., et al., Fus. Engin. and Design **65** (2003) 165.

[48] MAJESKI, R., DOERNER, R., GRAY, T., KAITA, R., MAINGI, R., et al., Phys. Rev. Lett. **97** (2006) 075002.

[49] MAJESKI, R., KUGEL, H., BELL, M., BUSH, C., DOERNER, R., et al., Paper EX/P4-23, this conference.

[50] RAMAN, R., NELSON, B. A., BELL, M. G., JARBOE, T. R., MUELLER, D., et al., Phys. Rev. Lett. (2006), to appear in October.

[51] RAMAN, R., JARBOE, T. R., MUELLER, D., NELSON, B. A., BELL, M. G., et al., Paper EX/P8-16, this conference.

[52] BIEWER, T. M., BELL, R. E., DIEM, S. J., PHILLIPS, C. K., WILSON, J. R., et al., Phys. Plasmas **12** (2005) 056108.

[53] LEBLANC, B. P., BELL, R. E., KAYE, S. M., STUTMAN, D., BELL, M. G., et al., Nucl. Fus. **44** (2004) 513.

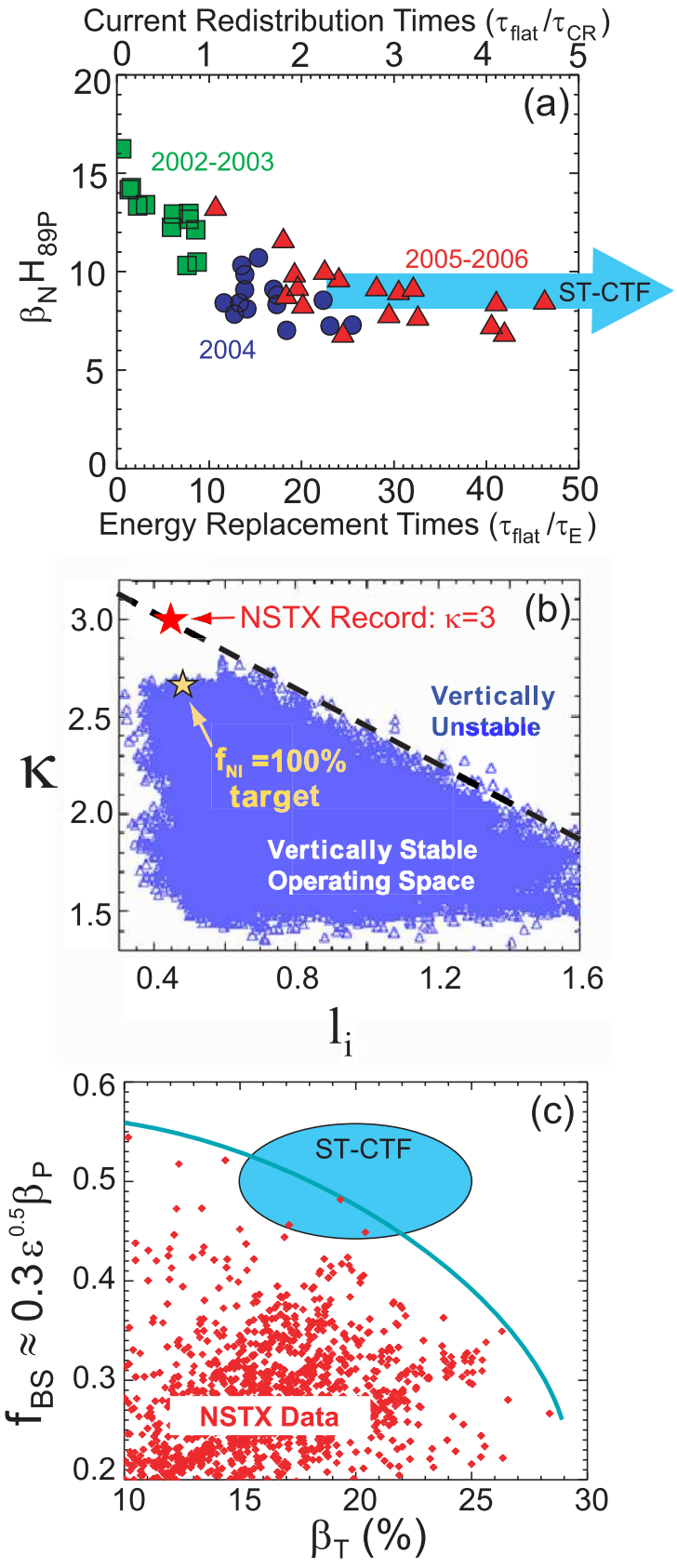


*Figure 1: (a) $\beta_N \times H_{89P}$ vs. normalized pulse length, (b) peak elongation vs. internal inductance, and (c) peak estimated bootstrap fraction vs. toroidal beta.*

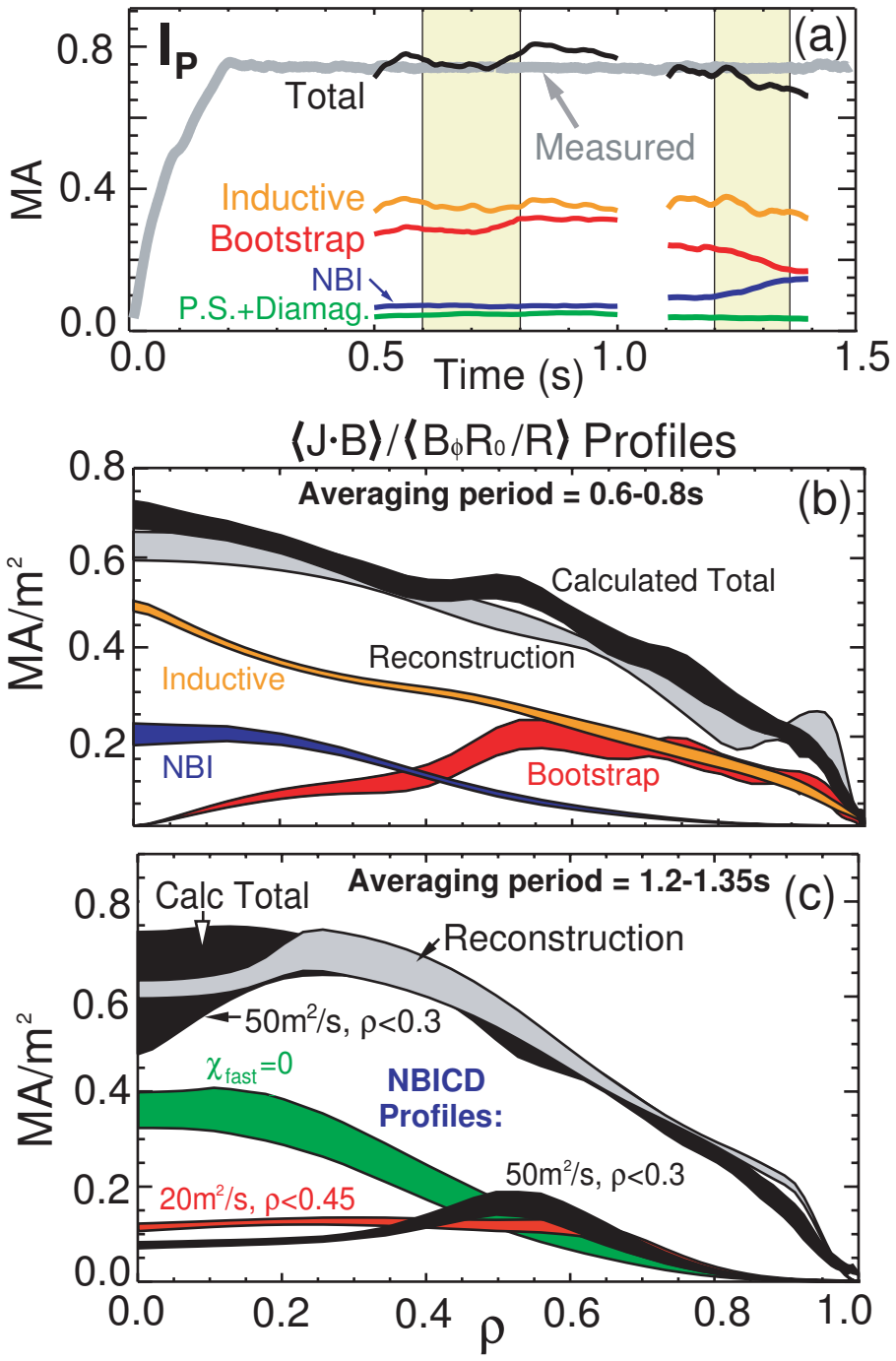


*Figure 2: (a) Comparison of predicted and measured total current, (b) comparison of measured and reconstructed current density profiles during high β, MHD-quiescent phase, and (c) evidence for MHD-induced NBICD diffusion.*

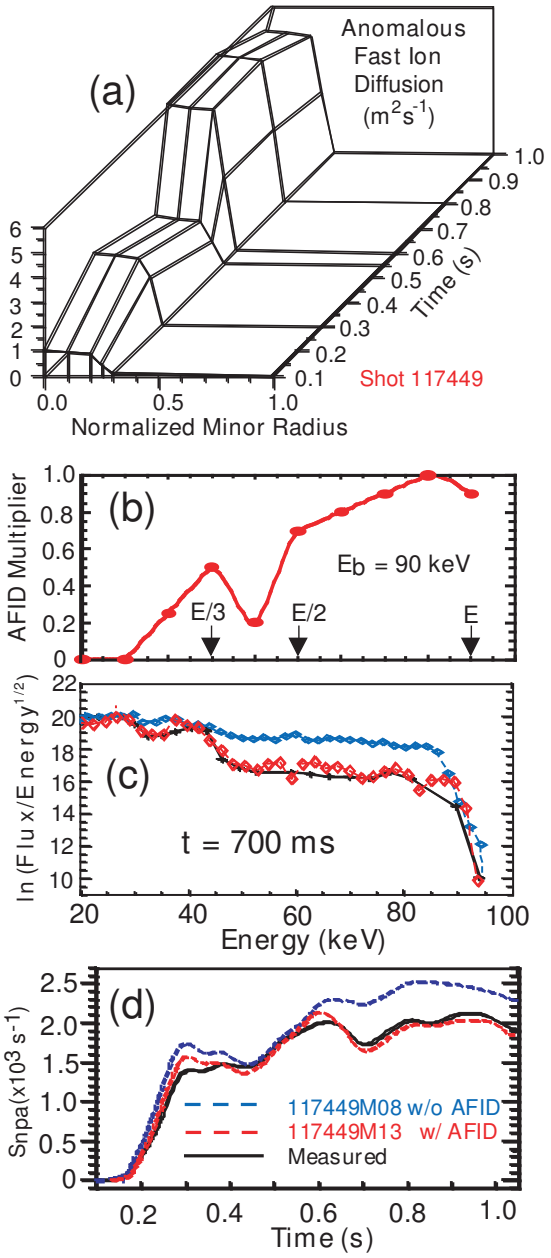


*Figure 3: (a) Time-dependent profile of anomalous fast ion diffusion (AFID) used to simulate fast ion redistribution by low-frequency MHD activity for a discharge similar to that shown in Figure 2, (b) energy dependence of the AFID model, (c) improved agreement with measured NPA energy spectrum with AFID model included, and (d) comparison of the measured and simulated NPA signal with and without AFID.*

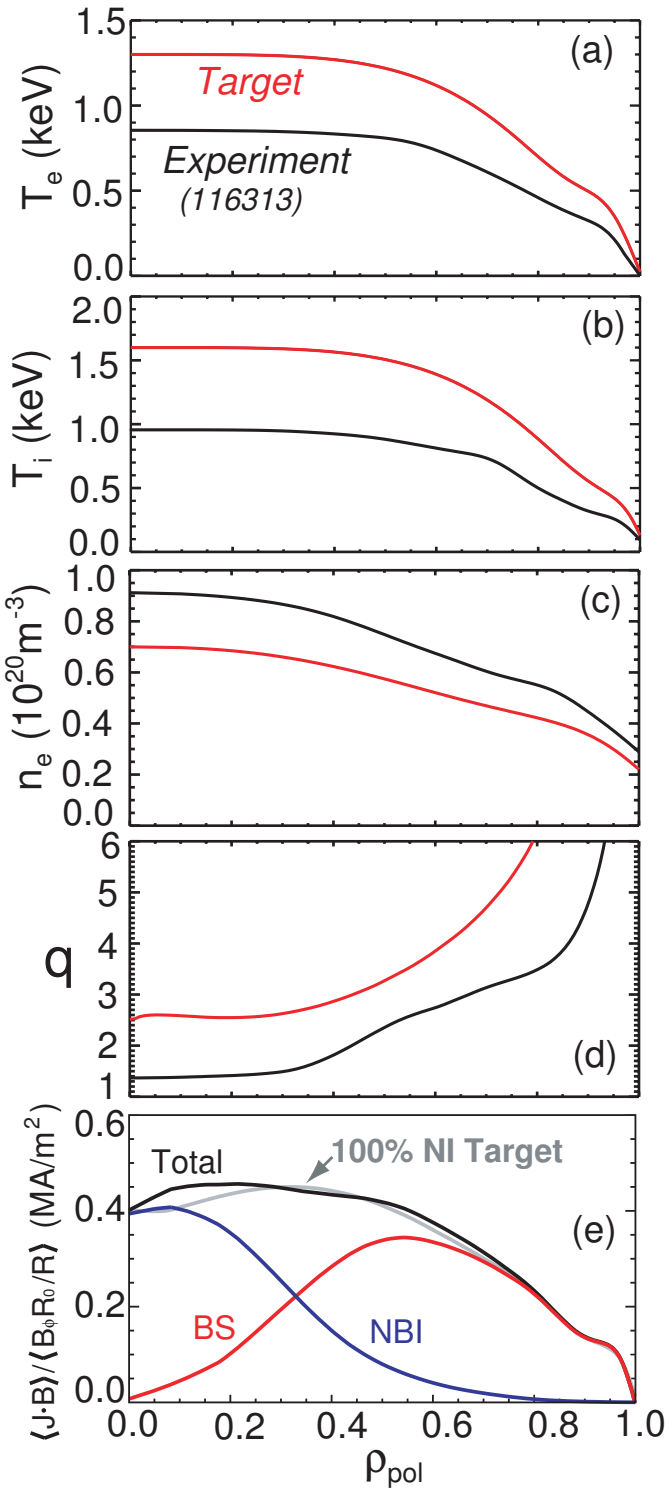


*Figure 4: Present experimental profiles (black) and profiles needed (red) to achieve a fully non-inductive target equilibrium utilizing only NBI and BS current. (a) Electron temperature, (b) ion temperature, (c) electron density, (d) safety factor profile, and (e) parallel current density profiles (for the fully non-inductive target equilibrium).*

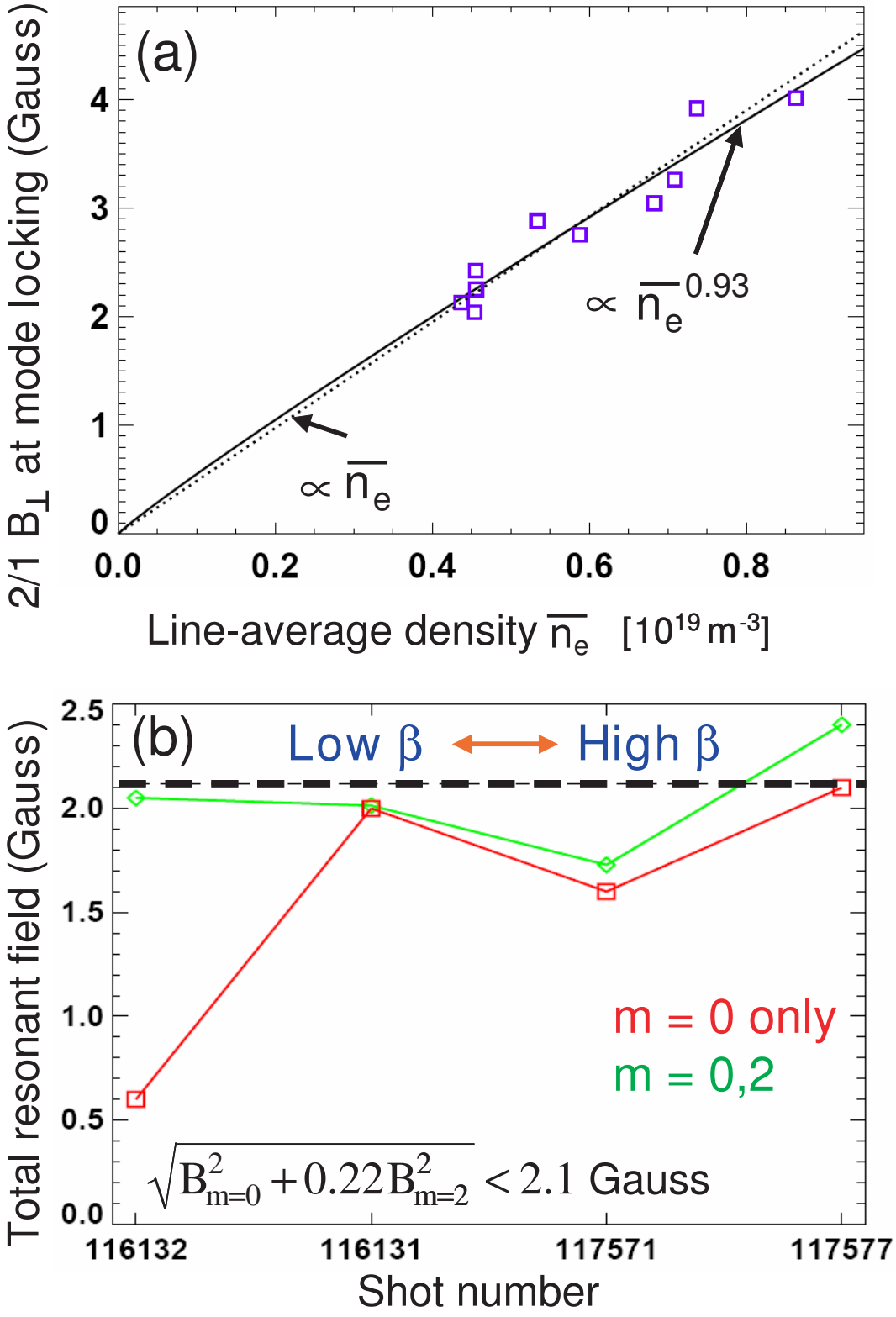


*Figure 5: (a) density scaling of the 2/1 component of the flux-surface-normal B-field amplitude at locked-mode onset versus line-average density, and (b) total (intrinsic+applied) error field threshold calculated at the q=3 surface at the onset of locking (low β) and rotation collapse (high β).*

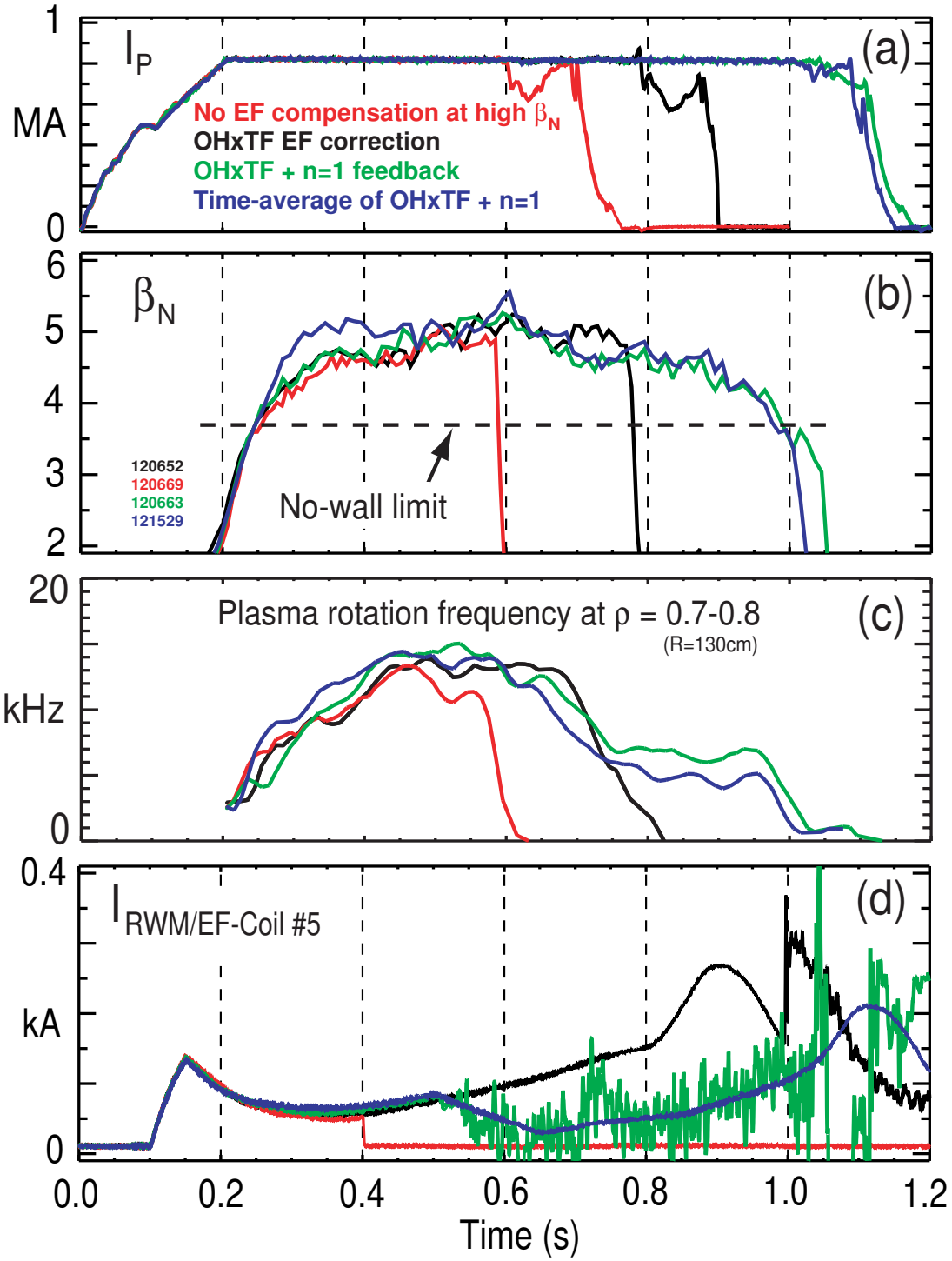


*Figure 6: (a) Plasma current, (b) normalized beta, (c) plasma rotation near q=2 and 3 surfaces, and (d) RWM/EF coil current during dynamic error field correction experiments.*

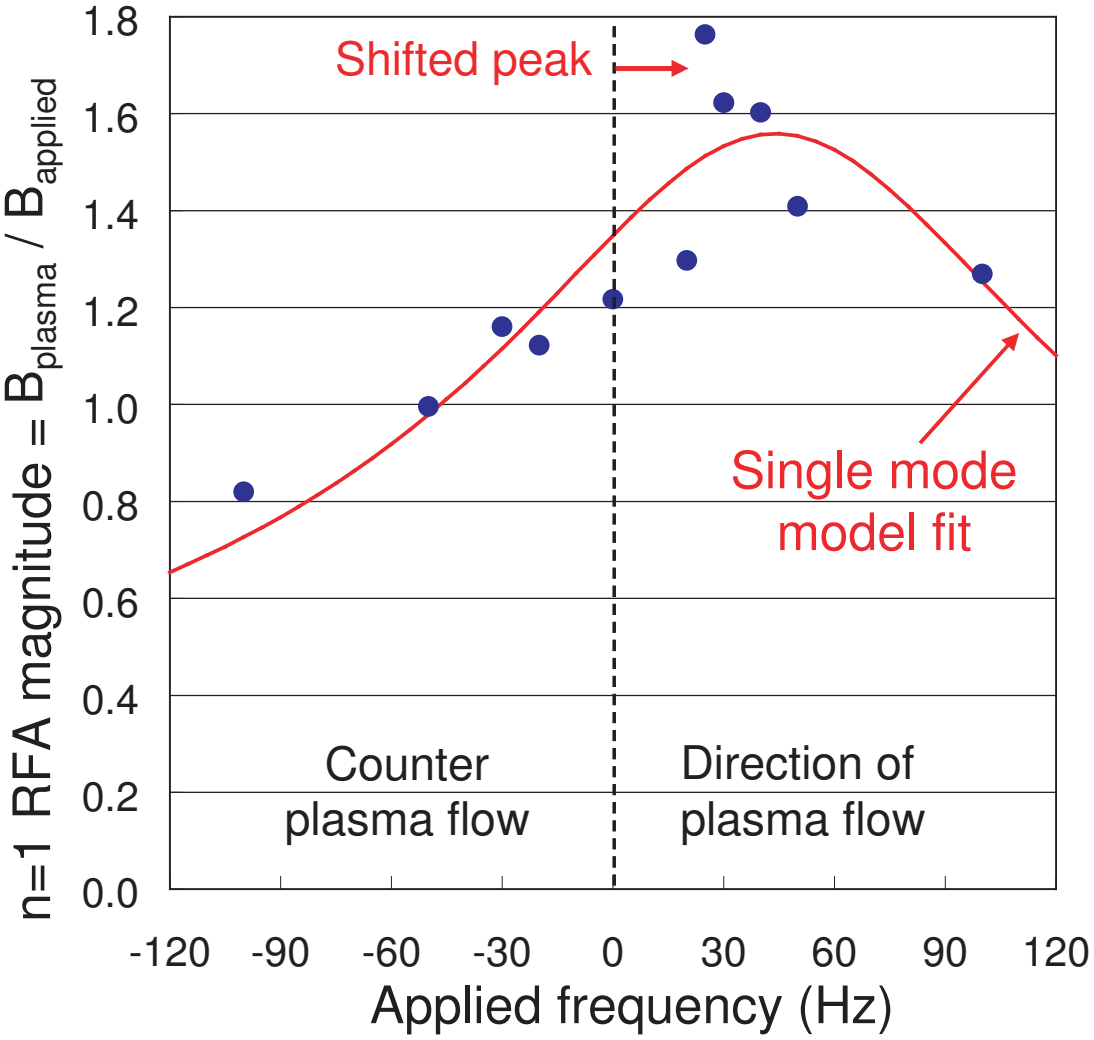


*Figure 7: Resonant field amplification (RFA) versus applied frequency of n=1 traveling waves excited using the midplane mode-control coils of NSTX in a plasma operating above the n=1 no-wall stability limit.*

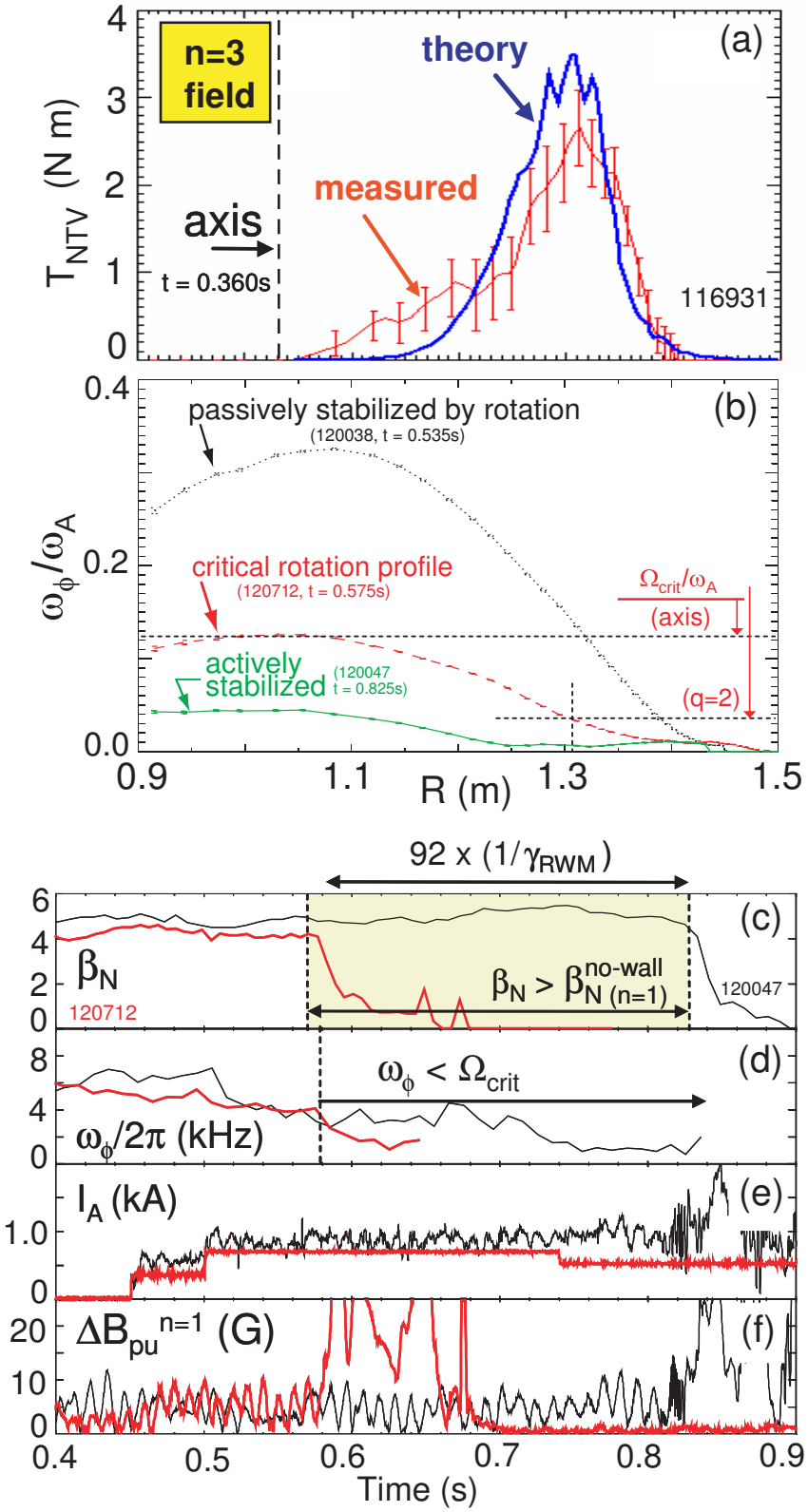


*Figure 8: (a) Torque comparison, (b) plasma rotation profiles, and evolution of (c) normalized beta, (d) rotation, (e) RWM/EF coil current, and (f) mode n=1 poloidal field for magnetic braking and RWM feedback experiments.*

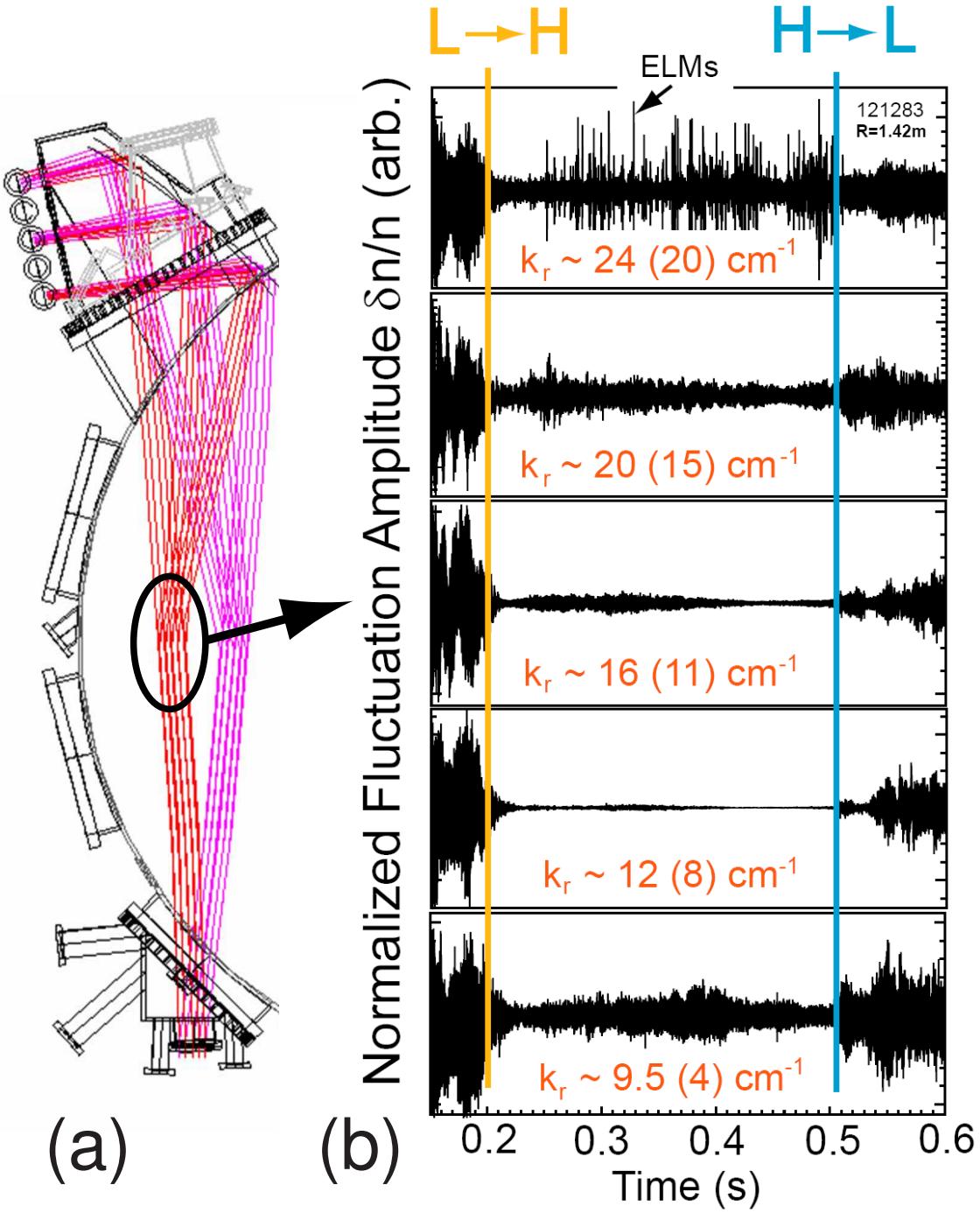


*Figure 9: (a) Radially scannable high-k scattering diagnostic as viewed from above, (b) $\delta n/n$ fluctuation levels (renormalized to initial L-mode values) in L-mode and H-mode of a $P_{NBI}$=2MW, $I_P$=0.8MA, $B_T$=0.45T discharge for a range of radial wavenumbers. Wavenumbers before parentheses are for the H-mode phase, while numbers in parentheses are for the L-mode phase.*

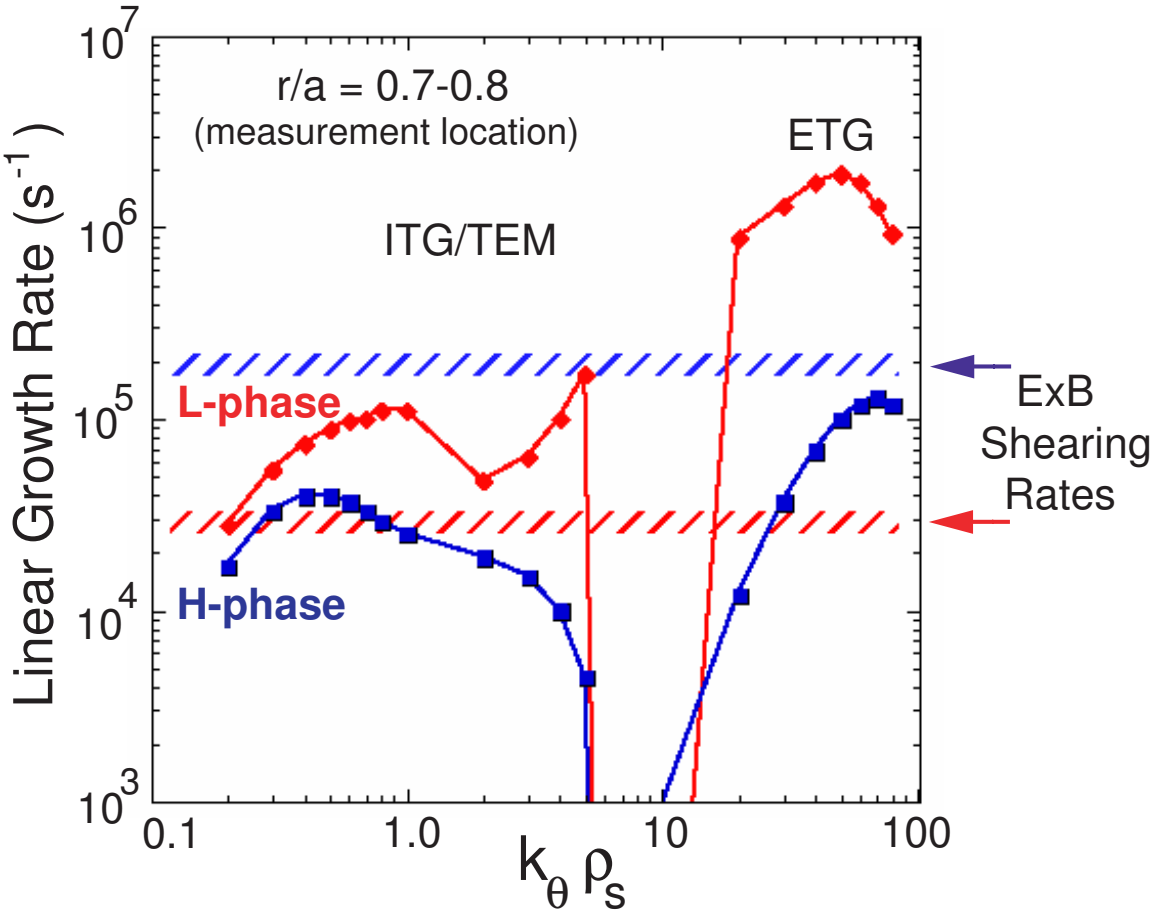


*Figure 10: Linear growth-rates of ITG/TEM ($k_\theta \rho_s < 10$) and ETG ($k_\theta \rho_s > 10$) micro-instabilities versus normalized poloidal wavenumber calculated with the GS2 gyro-kinetic code for the early L-mode (red) and H-mode (blue) phases of the discharge shown in Figure 9. The $E \times B$ shearing rates for the H-mode and L-mode discharge phases are also shown for comparison to the linear growth rates.*

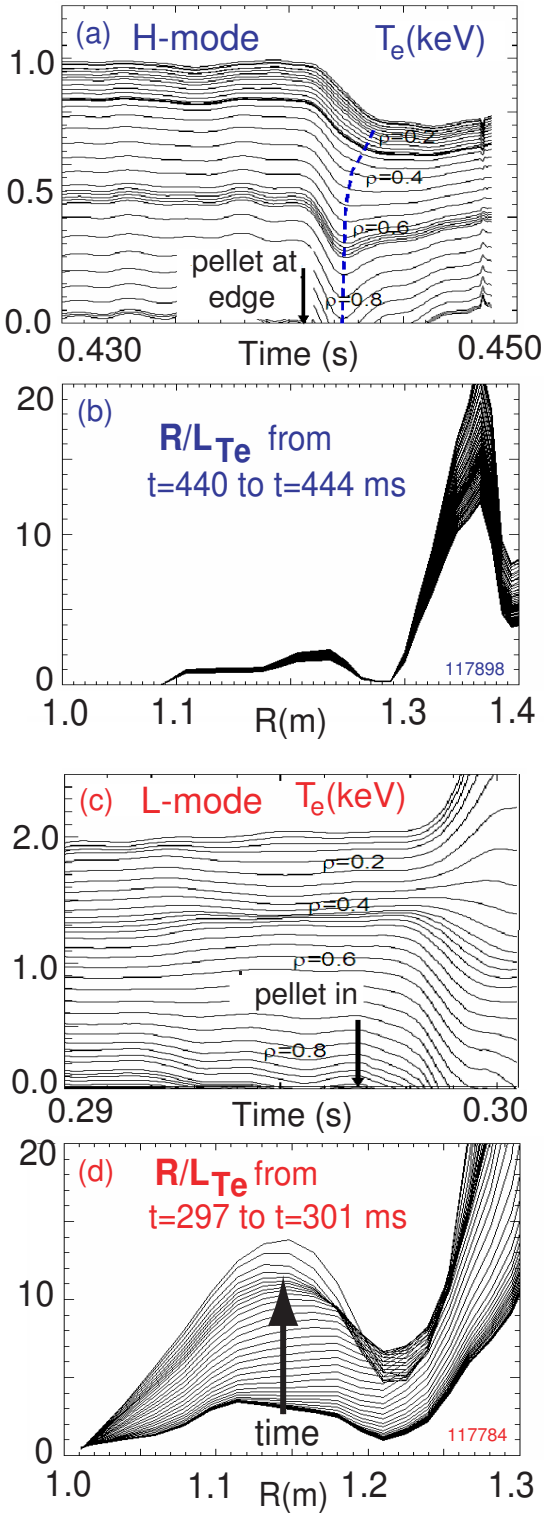


*Figure 11: (a) $T_e$ and (b) $T_e$ gradient evolution in H-mode, and (c) $T_e$ and (d) $T_e$ gradient evolution in L-mode during edge perturbations induced by lithium pellet injection.*

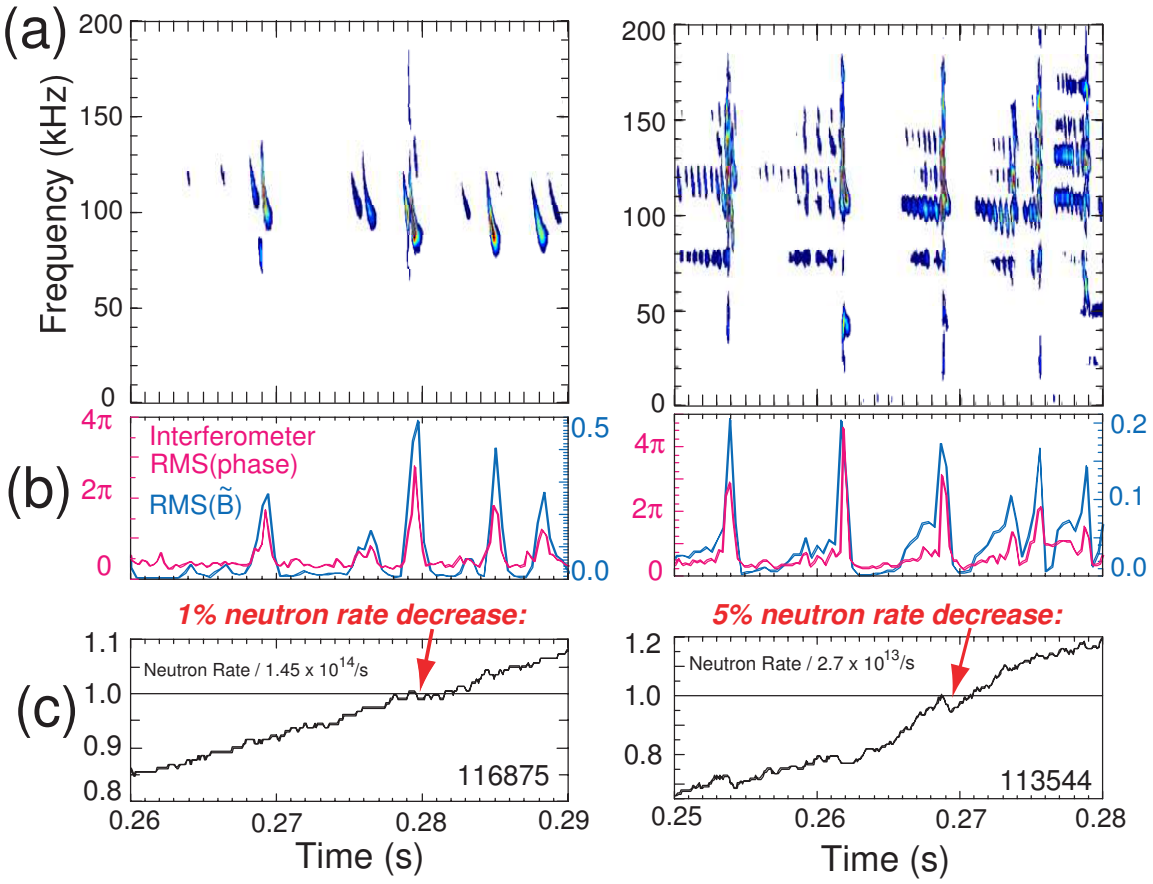


*Figure 12: (a) Mode frequency spectra, (b) density fluctuation and Mirnov oscillation amplitudes, and (c) neutron rate decrements during single-mode TAE (left) and multi-mode TAE (right) bursts.*

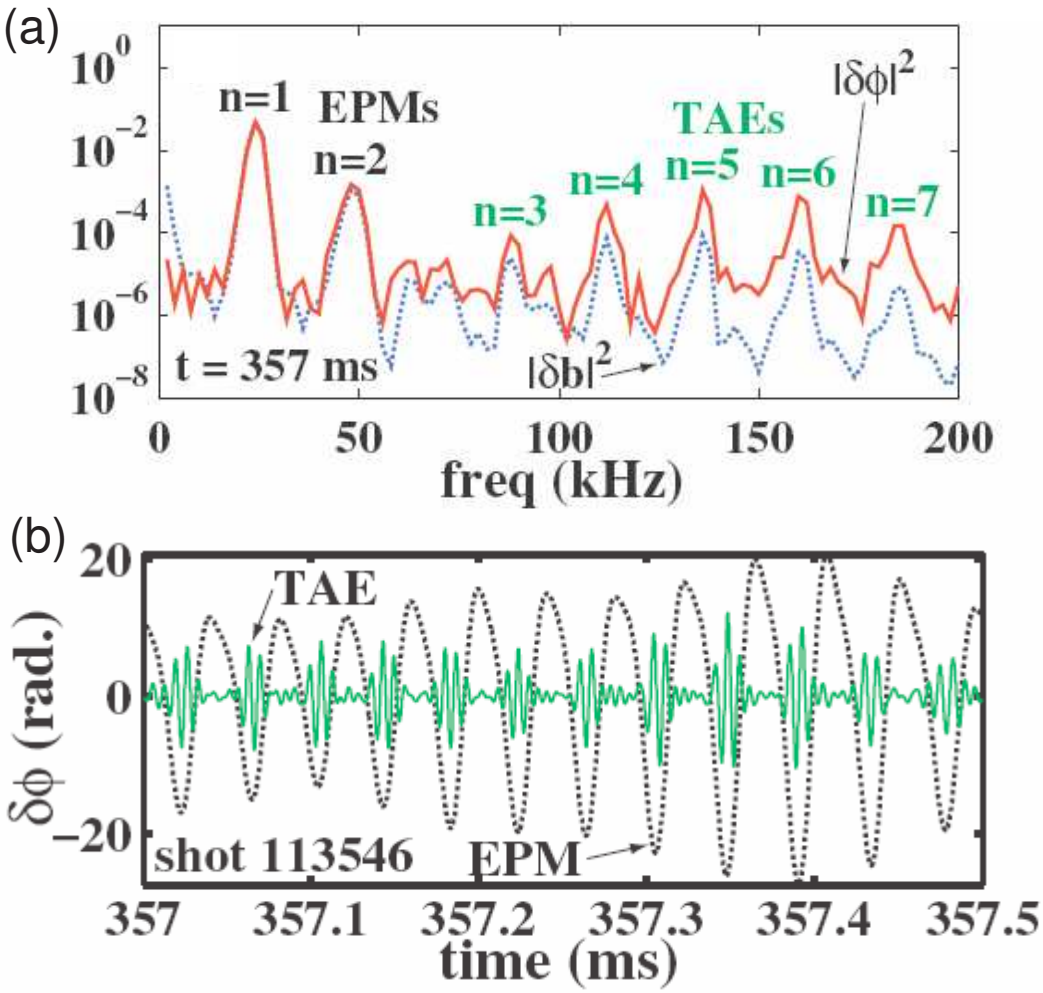


*Figure 13: (a) Mirnov and reflectometer spectra showing multiple EPM and TAE modes, and (b) toroidal localization of TAE amplitude envelope from 3-wave coupling to n=1 EPM.*

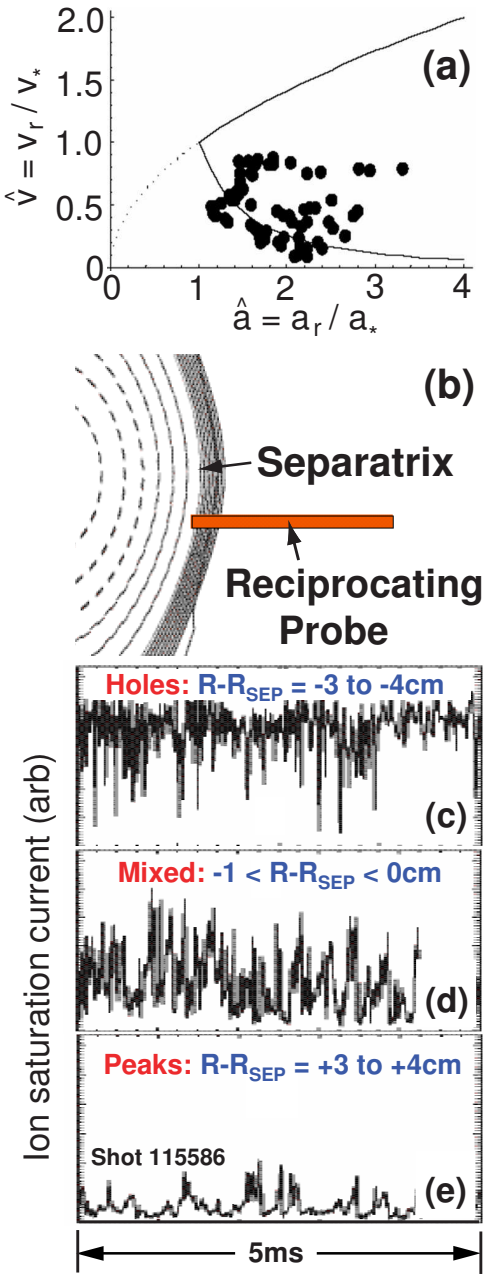


*Figure 14: (a) Measured (circles) "blob" normalized radial velocity versus normalized radial scale-size compared to predicted bounds (lines), (b) edge reciprocating probe position relative to plasma boundary, (c) ion saturation current fluctuations far inside separatrix, (d) just inside separatrix, and (c) outside separatrix in scrape-off-layer (SOL).*

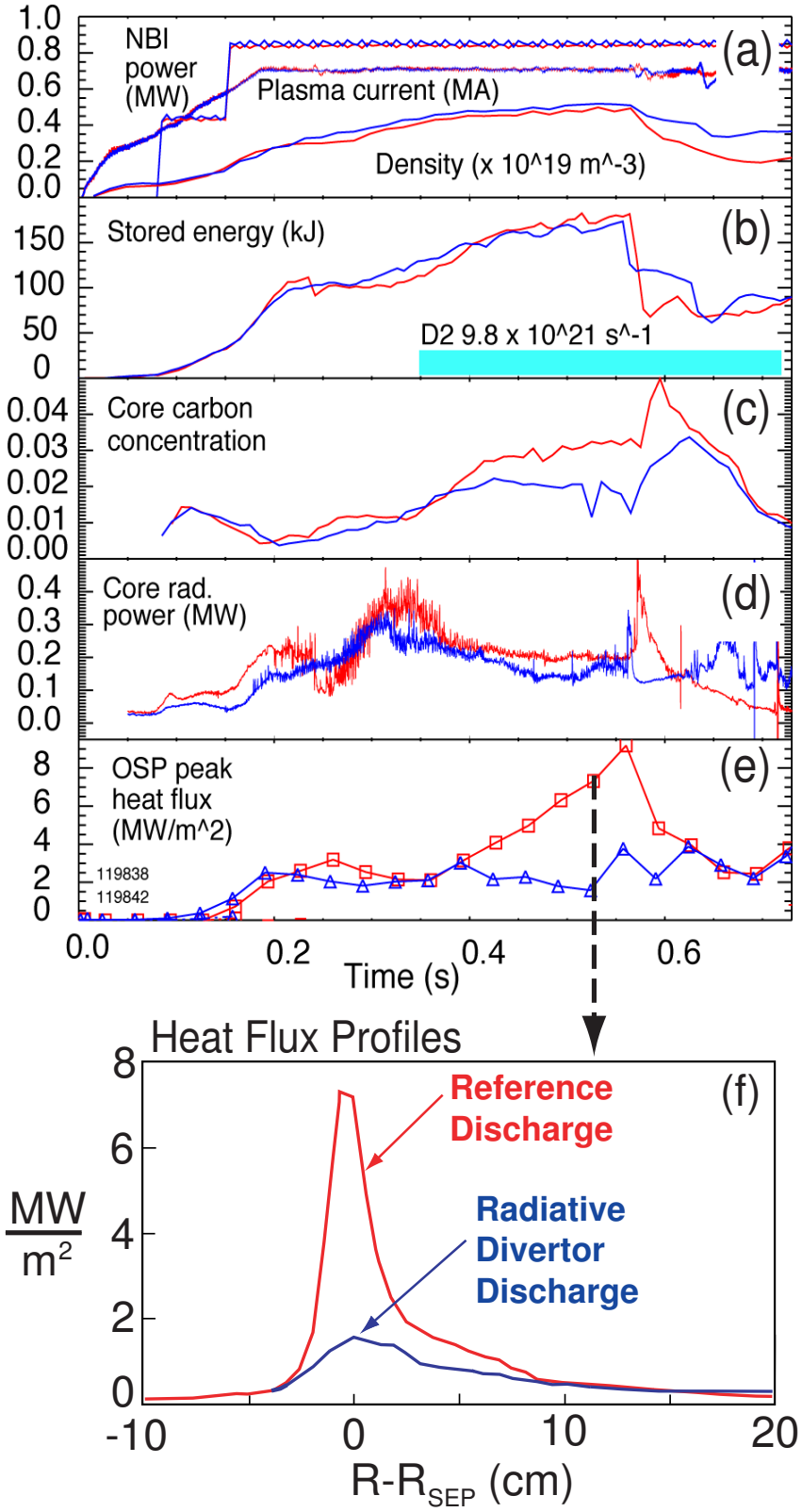


*Figure 15: Time evolution of (a) $I_P$, line-average density, and NBI heating power, (b) plasma stored energy, (c) core carbon concentration, (d) core radiated power, (e) peak divertor heat flux, and (f) radial profile of divertor heat flux for reference and radiative divertor discharges.*

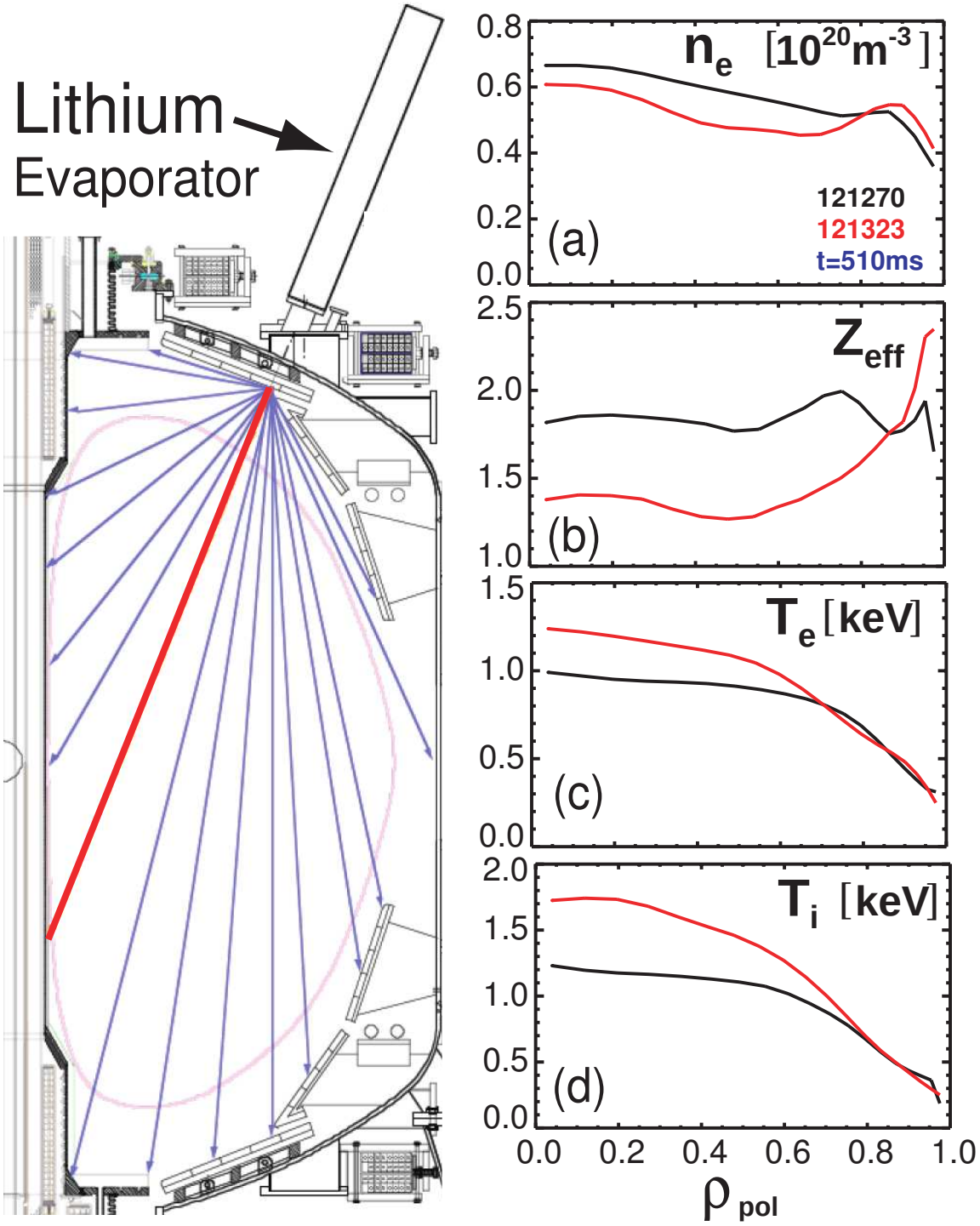


*Figure 16: Comparisons of (a) $n_e$, (b) $Z_{eff}$, (c) $T_e$, and (d) $T_i$ before (black) and after (red) lithium evaporation conditioning.*

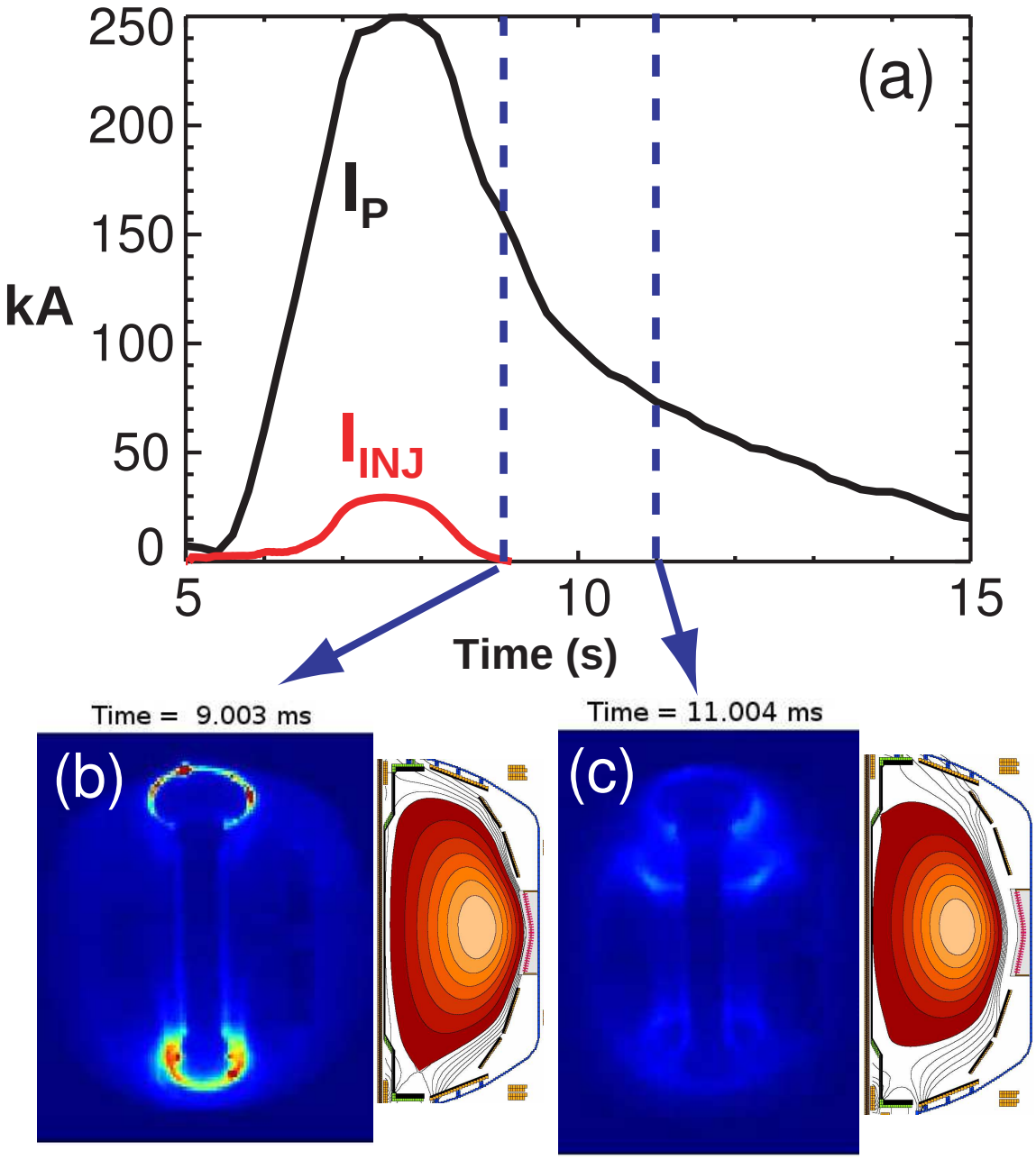


*Figure 17: (a) Plasma and injector currents vs. time, and fast-camera images and flux-surface reconstructions at (b) peak closed-flux $I_P$ and (c) during $I_P$ decay.*

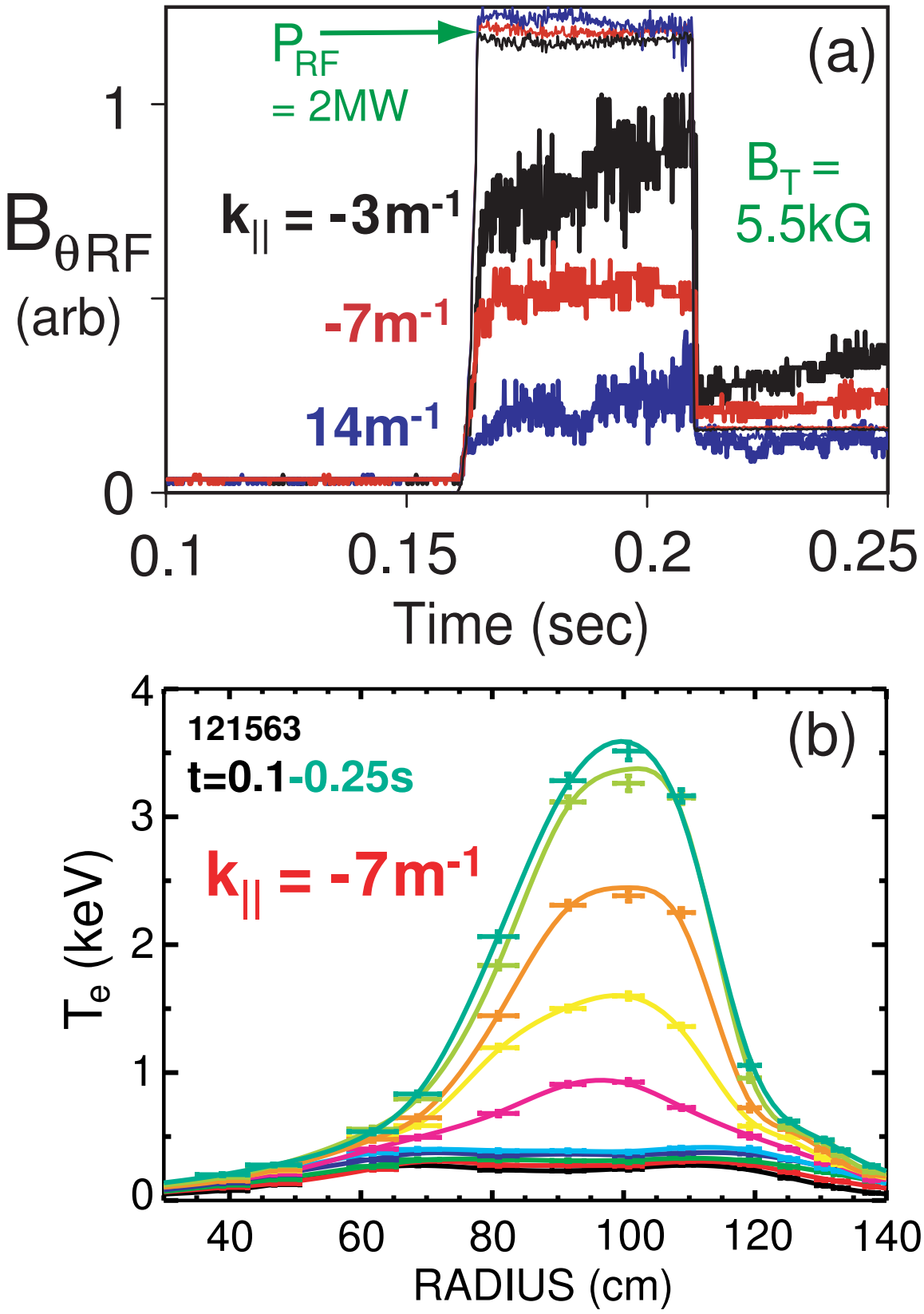


*Figure 18: (a) Far-field HHFW $B_\theta$ amplitude vs. launched $k_{||}$, and (b) $T_e(t, R)$ for an $I_P$ = 700kA $B_T$ = 5.5kG target plasma heated with 2MW of HHFW.*

The Princeton Plasma Physics Laboratory is operated
by Princeton University under contract
with the U.S. Department of Energy.

Information Services
Princeton Plasma Physics Laboratory
P.O. Box 451
Princeton, NJ 08543

Phone: 609-243-2750
Fax: 609-243-2751
e-mail: pppl_info@pppl.gov
Internet Address: http://www.pppl.gov